JGR Solid Earth

RESEARCH ARTICLE

Key Points:

- We conduct 3D dynamic rupture simulations for the future possible scenarios in Cascadia with constraints from interseismic locking models
- Different hypocenters in southern Cascadia reveal rupture segmentation and the southernmost unilateral rupture gives greater ground-shaking
- Our dynamic rupture scenarios have reasonably consistent segmentation extents and coastal subsidence patterns with paleoseismic observations

Supporting Information:

Supporting Information may be found in the online version of this article.

Correspondence to:

H. Yang,
hyang@cuhk.edu.hk

Impact of Hypocenter Location on Rupture Extent and Ground Motion: A Case Study of Southern Cascadia

Yuk Po Bowie Chan[1] [ID]**, Suli Yao[1]** [ID]**, and Hongfeng Yang[1,2]** [ID]

[1]Earth and Environmental Sciences Programme, The Chinese University of Hong Kong, Hong Kong, China, [2]Shenzhen Research Institute, The Chinese University of Hong Kong, Shenzhen, China

Abstract The Cascadia subduction zone has well-documented geological records of megathrust earthquakes with the latest $\sim M_w$ 9 rupture occurring in CE 1700. The paleoseismic observations suggest that southern Cascadia is mature for future earthquakes since the last event. Consequently, it is crucial to investigate the potential rupture scenarios. Although existing interseismic locking models share similar moment deficits, whether future earthquakes would be margin-wide or segmented, as suggested by paleoseismic records, remains unknown. Accordingly, we aim to investigate: (a) possible rupture segmentation patterns, (b) whether south Cascadia can host margin-wide ruptures, and (c) whether the existing locking models suggest similar future rupture scenarios. Assuming constant effective normal stress, we estimate the stress distribution constrained by the locking models (i.e., Gamma model from Schmalzle et al. (2014, https://doi.org/10.1002/2013GC005172), the preferred model from S. Li et al. (2018, https://doi.org/10.1029/2018JB015620), and the best-fit model from Lindsey et al. (2021, https://doi.org/10.1038/s41561-021-00736-x)) from static calculation and discover they lead to different stress distributions, indicating distinct seismic potentials. Our dynamic rupture scenarios show that the south can generate both segmented ruptures ($> M_w$ 7.3–8.4) and margin-wide ruptures ($> M_w$ 8.6) depending on the hypocenter location. The along-strike rupture length appears to coincide with rupture lengths hypothesized from paleoseismology, and the Schmalzle model produces reasonable coastal subsidence amplitudes from the CE 1700 event. Therefore, we propose that three high-slip trench-breaching patches are sufficient for reproducing historical subsidence records. Our results can be further applied in seismic and tsunami hazard assessment, and serve as a comparison for non-trench-breaching scenarios.

Plain Language Summary The Cascadia subduction zone is a region off the coast of North America where one tectonic plate (Juan de Fuca) slowly slides beneath another (North America). Although there have been no significant earthquakes in Cascadia recently, geological records indicate that the last earthquake, estimated as a magnitude 9, occurred in CE 1700. In between earthquake occurrences, stress is accumulated and manifested in strain build-up measurable by instruments. Existing models infer stress accumulation from these measurements but are variable along the length of the earthquake fault. Based on stress distributions suggested by the models, we design potential future earthquake scenarios using three-dimensional computer simulations. Our results show how the final earthquake size and expected ground-shaking change depending on where it is allowed to initiate in the simulation.

1. Introduction

The Cascadia subduction zone is known to host great megathrust earthquakes as large as moment magnitude (M_w) 9 (Walton et al., 2021; K. Wang and Tréhu, 2016). Based on paleoseismic records, the average recurrence intervals of these events are variable but may extend to about 500 years (Engelhart et al., 2015; Goldfinger et al., 2012; Kelsey et al., 2005; Long and Shennan, 1998). It has been over 322 years since the latest great earthquake, an $M \sim 9$ margin-wide rupture in CE 1700 accompanied by a large, trans-Pacific tsunami (Atwater & Hemphill-Haley, 1997; Goldfinger et al., 2012, 2017; Satake et al., 2003). Modern interseismic geodetic observations estimate substantial slip deficit rate, which indicates strain energy accumulation, along almost the entire Cascadia margin toward a future earthquake (Burgette et al., 2009; Flück et al., 1997; S. Li et al., 2018; Lindsey et al., 2021; McCaffrey et al., 2013; Michel et al., 2019; Pollitz and Evans, 2017; Schmalzle et al., 2014; K. Wang et al., 2003).

One challenge in seismic hazard assessment at Cascadia is estimating the potential of rupture segmentation along the megathrust. There are questions regarding whether past events were predominantly full-margin ruptures

(FMR) or sequences of smaller ruptures that were too closely spaced in time to be resolved by paleoseismic records (Atwater et al., 2014; Frankel et al., 2015; Melgar, 2021; P. L. Wang et al., 2013). Along-strike heterogeneities in megathrust and crustal structure are thought to have the potential to cause rupture segmentation in various parts of the margin (Tréhu et al., 2012; K. Wang and Tréhu, 2016; Watt and Brothers, 2021). Based on the interpretation of offshore turbidity records, megathrust earthquakes occurred more frequently in southern Cascadia, especially south of Cape Blanco (Goldfinger et al., 2017). The average recurrence interval is inferred to increase from around 200 years in the south to around 300 years in the central segment and 400–500 years in the north (Goldfinger et al., 2017; Witter et al., 2012). If the CE 1700 event was a FMR as inferred by Satake et al. (2003), then at present the short-recurrence southern segment is statistically expected to be more ready for the next rupture. The first scientific question we address in this study is if a megathrust earthquake nucleates in southern Cascadia, what physical conditions promote FMR?

Dynamic rupture scenarios based on interseismic locking models can contribute to estimating the magnitude, rupture extent, and potential segmentation of future earthquakes (D. Li & Liu, 2021; Ramos et al., 2021; S. Yao and Yang, 2022; Yang, Yao, He, Newman, Weng, 2019). For instance, Yang, Yao, He, Newman, Weng (2019) derived dynamic scenarios for the Costa Rica subduction zone by using interseismic locking models to derive the initial stress of the megathrust prior to the rupture and were able to explain the rupture extent and magnitude of the 2012 Nicoya M_w 7.6 earthquake. Using a similar approach, Ramos et al. (2021) conducted dynamic rupture simulations for Cascadia with the initial stress based on the interseismic locking model of Schmalzle et al. (2014). By nucleating ruptures from a high-stress location either in the south or in the north, they obtained scenarios of margin-wide rupture. D. Li and Liu (2021) conducted quasi-dynamic numerical simulation of long-term fault behavior in Cascadia. They inferred fault rate-state friction stability from interseismic locking models (Burgette et al., 2009; Schmalzle et al., 2014). They found that whether the rupture was full-margin depended on what locking model was used.

Besides rupture extent and earthquake magnitude, the effect of rupture directivity on ground motion should be further investigated using dynamic rupture simulations. With a heterogeneous initial stress distribution along the fault, different hypocenter locations can lead to different rupture directivities (Yang, Yao, He, Newman, 2019; S. Yao and Yang, 2022). Even with a similar rupture extent, a different rupture directivity leads to a very different pattern of ground motion intensity (S. Yao and Yang, 2022). Therefore, the second scientific question we address in this study is how hypocenter location controls rupture directivity to impact ground motion.

To investigate the above questions, we carry out dynamic rupture simulation to obtain self-consistent rupture scenarios. We consider different Cascadia megathrust locking models (Figure 1), namely those by Schmalzle et al. (2014), S. Li et al. (2018), and Lindsey et al. (2021). Our research aims to derive rupture scenarios originating from South Cascadia. Assuming the same stress accumulation time and constant effective normal stress, we investigate the role of stress distribution and hypocenter location in producing possible segmentation ground motion patterns. We further compare the rupture scenarios with the proposed segmented paleoearthquakes as well as coseismic subsidence amplitudes.

2. Interseismic Locking Models of the Cascadia Megathrust

Since solutions for the inversion of geodetic measurements are nonunique, different assumptions are applied in deriving interseismic locking models, governing the smoothness of slip distribution and the degree of locking at the trench (S. Li et al., 2018; Lindsey et al., 2021; McCaffrey et al., 2013; Michel et al., 2019; Pollitz and Evans, 2017; Schmalzle et al., 2014). Here we summarize the three locking models adopted in this work, all derived by inverting land-based GNSS observations (Figure 1). Although Cascadia does not have a geomorphological trench because of the thick sediment cover, we refer to the deformation front as the "trench" in the following discussion for wording convenience.

Because land-based GNSS measurements cannot resolve the locking state of the shallowest portion of the megathrust which is far offshore, Schmalzle et al. (2014), following McCaffrey et al. (2013), proposed two models of opposite, prescribed near-trench locking states which fit the GNSS data equally well. One model assumes full locking at the trench with the locking degree monotonically decreasing downdip following the Gamma function designed by K. Wang et al. (2003) (Gamma model). The other model assumes a Gaussian-like locking distribution so that creeping occurs at the trench and full locking occurs farther downdip (Gaussian model). Almeida
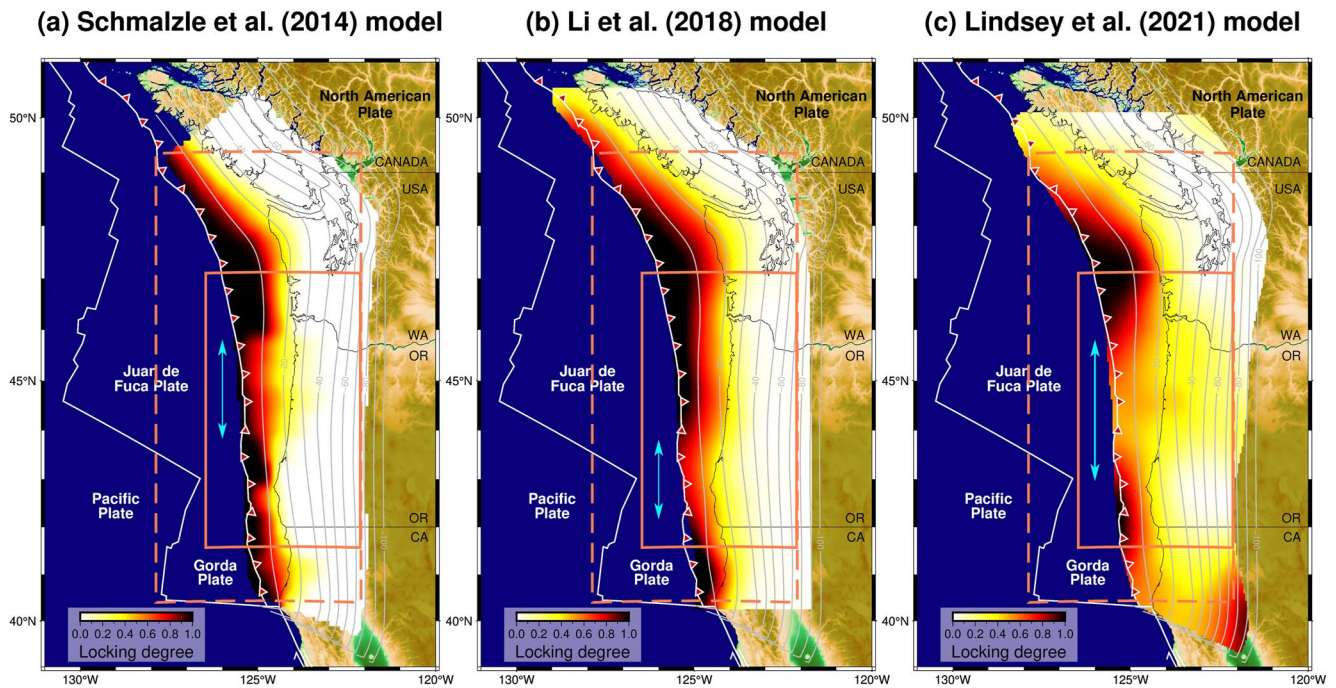
Figure 1. Interseismic locking models for the Cascadia megathrust. (a) Model from Schmalzle et al. (2014). (b) Model from S. Li et al. (2018). (c) Model from Lindsey et al. (2021). Coral dashed line: our static calculation domain. Coral solid line: our dynamic simulation domain. Cyan arrow: central creeping segments.

et al. (2018) and Lindsey et al. (2021) propose that many geodetic models possibly underestimated the degree of shallow coupling due to stress shadowing effects. Thus, in this study, we only use the Gamma model, referred to as the Schmalzle model hereafter (Figure 1a).

Following the explanation of Almeida et al. (2018), Lindsey et al. (2021) included in their locking model the effect of stress shadowing in which a frictionally unlocked shallow segment of the fault may have little motion because of the neighboring frictionally locked patches immediately downdip. Although stress shadowing is explicitly invoked, the kinematic behavior of the megathrust in this model is similar to that described by the aforementioned Gamma model. The difference in inversion results is caused mainly by assumed inversion parameters that constrain slip deficit distribution. In this study, we use their best-fit locking model, referred to as the Lindsey model (Figure 1c).

The above two locking models assume an elastic Earth, but the real Earth is viscoelastic, and viscoelastic stress relaxation plays an important role not only in postseismic but also interseismic deformation (K. Wang et al., 2012). To address this effect, Pollitz and Evans (2017) and S. Li et al. (2018) inverted Cascadia interseismic geodetic data based on analytical solutions and finite element models, respectively. S. Li et al. (2018) constructed many locking models that fit the geodetic data equally well. Here we only use their "preferred" locking model, referred to as the Li model (Figure 1b).

Because of the lack of near-field, seafloor geodetic constraints, all these models suffer from a high degree of nonuniqueness and thus contain large errors. By using these models to design initial fault stress distribution, we do not intend to construct a "correct" dynamic rupture model. Instead, we use these models to explore how different initial stress distributions may affect the rupture process. As such, these models may be considered ad-hoc to each other. An improved understanding of the dynamic rupture process will help the design of kinematic rupture models for the purpose of probabilistic seismic hazard analyses and the appraisal of model uncertainties. We think the three models shown in Figure 1 adequately represent the range of assumptions used in constructing Cascadia megathrust locking models by different research groups in terms of Earth rheology, near-trench locking state, and smoothness of slip deficit distribution. Since stress accumulation is mostly determined by the spatial gradient of the locking distribution and the major first-order features of active faulting could be governed by the spatial gradients of stress (Nur, 1978), it is important to ask whether the slip deficit heterogeneities in these locking models can lead to consistent rupture scenarios.
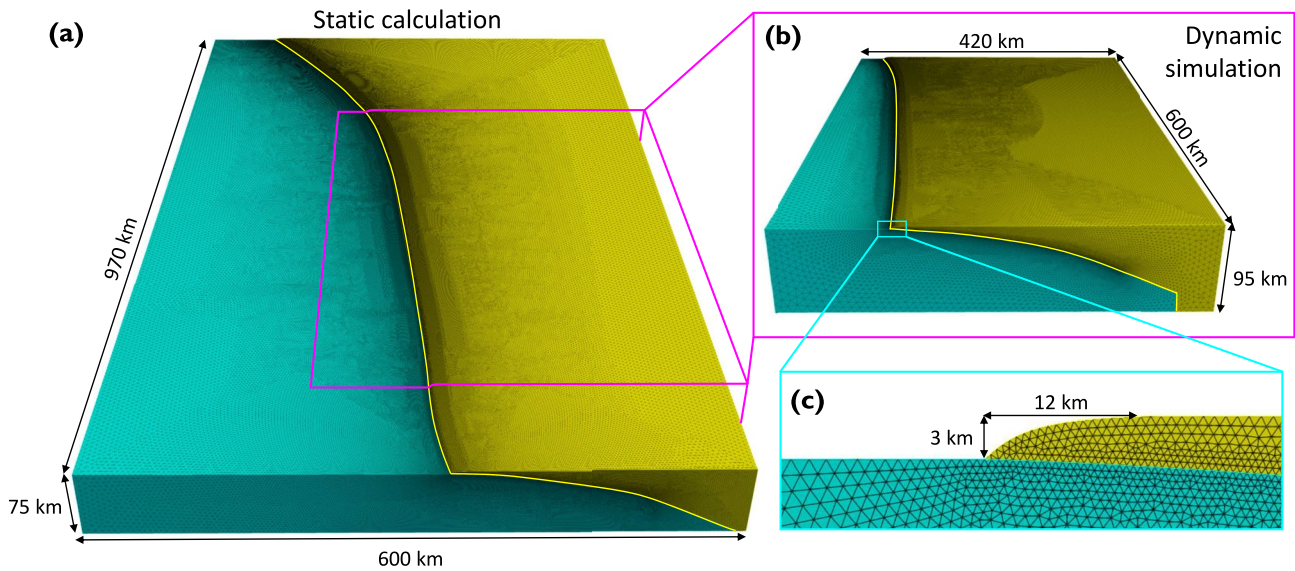
Figure 2. 3D model configuration. (a) Finite element mesh for static calculation with two model units: oceanic block (cyan) and continental block (yellow). (b) Finite element for the dynamic simulations. (c) Mesh geometry near the trench—continental block edge approximated with an exponential curve away from the trench.

3. Method and Model Parameter

We use open-source finite-element code PyLith v2.1.0 which is developed for dynamic and quasi-static simulations of crustal deformation (Aagaard et al., 2013c). Input parameters for our dynamic simulation include fault geometry, material properties, initial stresses (τ_0), and fault frictional law parameters (Harris et al., 2018).

3.1. Megathrust Geometry and Mesh

We adopt the Cascadia megathrust model of McCrory et al. (2004), which has a smoothly curved geometry starting from a 5 km depth below sea level, and use an exponential curve to approximate the shape of the upper plate near the trench as shown in Figure 2c.

We generate two 3D tetrahedral meshes for Cascadia using geometry and mesh generation software CUBIT (Blacker et al., 2016) to accommodate scientific purposes and computational costs. Both meshes consist of two model units—the oceanic block and the continental block. We use the larger one of the two meshes, extending from 40.5°N to 49°N covering the whole megathrust (Figure 2) to calculate stress distribution from locking models. We apply a coordinate transformation to fix the origin at −129°E, 39°N. This larger mesh extends 970, 600, and 75 km in the strike, strike-normal, and depth dimensions, respectively (Figure 2a). The element size on the fault is 500 m above 35 km depth for the major locked zone and gradually increases downdip.

For computational efficiency, we use the smaller one of the two meshes, extending from 41.5°N to 47°N, to conduct dynamic rupture simulation in our area of focus. We focus mainly on the scenarios of rupture initiation in the south and on the effect of the central segment. Geological evidence of ruptures limited to northern Cascadia is elusive (Petersen et al., 2014), suggesting that ruptures breaking the northern segment might eventually develop into margin-wide ruptures. This is consistent with the higher stress accumulation in the north provided by most locking models (Burgette et al., 2009; S. Li et al., 2018; Lindsey et al., 2021; McCaffrey et al., 2013; Michel et al., 2019; Pollitz and Evans, 2017; Schmalzle et al., 2014) as well as the dynamic simulation results from Ramos and Huang (2019) and Ramos et al. (2021). The small mesh covers the entire southern and central Cascadia, extending 600, 420, and 95 km in the strike, strike-normal, and depth dimensions, respectively (Figure 2b). The element size is 500 m above 50 km depth and gradually increases further downdip.

To minimize potential artifacts due to mesh boundaries, we extend the small mesh for the dynamic simulation to 95 km depth and even deeper than the larger mesh for static calculation by 20 km. In comparison, interseismic locking occurs mostly shallower than 30 km depth (Figure 1) and, to be further explained in Sections 3.3 and 4.1, the model-predicted rupture propagation does not extend far beyond this depth because of a lack of inferred
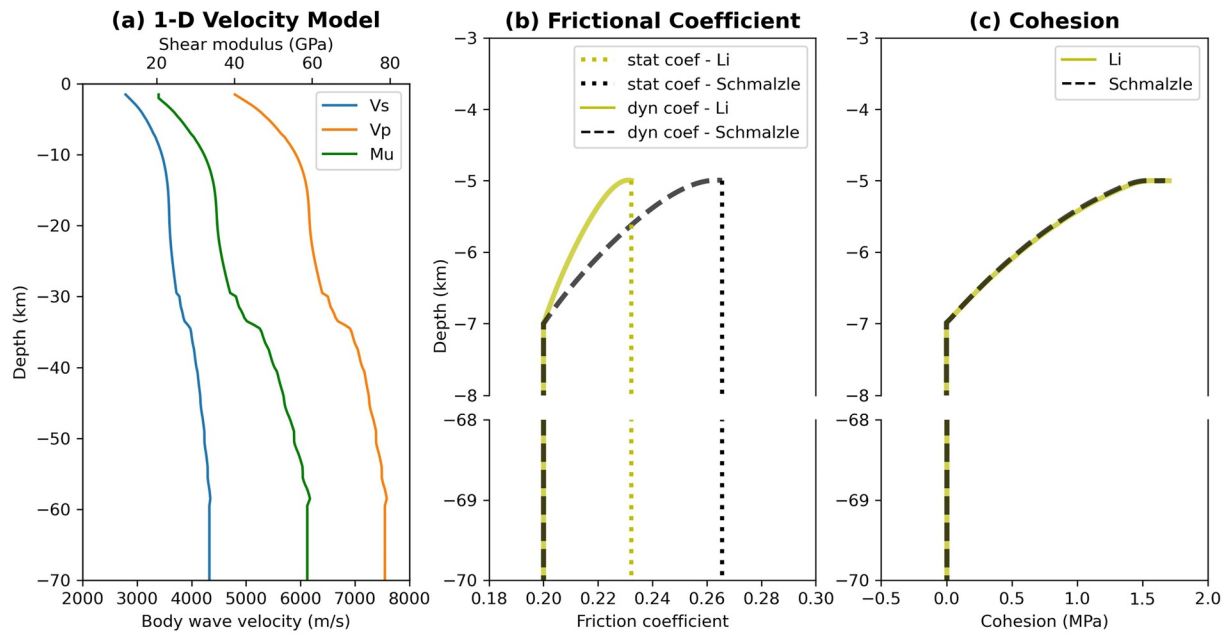
Figure 3. Depth-dependent parameters for dynamic rupture simulations. (a) 1-D velocity model calculated from Stephenson et al. (2017) and shear modulus. (b) Static coefficients are assumed constant throughout the whole megathrust while dynamic coefficients remain constant below 7 km depth. (c) Cohesion, remaining constant below 7 km depth.

interseismic stress built-up farther downdip. As will be shown in Section 4.2, none of our simulations features rupture deeper than 50 km depth.

3.2. Material Properties

Similar to most other dynamic rupture models, we assume an elastic Earth and apply absorbing conditions to all boundaries except the free surface at the top. The material property structure is based on the 3D Community Velocity Model of Cascadia (Stephenson et al., 2017) in which the body wave velocities of the oceanic block are approximately 30% higher than the continental block. The density is calculated from p-wave velocity based on the empirical relationship of Brocher (2005). We have tested two different material property structures in order to see how they affect the dynamic rupture process. One model is referred to as the 1-D velocity model, in which the material properties of the continental block are applied to the whole mesh. Another model is referred to as the bi-material velocity model, where material properties of both continental and oceanic blocks are considered (Figure S1). The two structures lead to very similar rupture scenarios. Between the two test models shown in Figure S2 in Supporting Information S1, the moment magnitude differs only by 0.01 (Figure S2 in Supporting Information S1). Hence, we use the 1-D velocity structure for the rest of our dynamic simulations (Figure 3a).

3.3. Stress Accumulation and Initial Stress on the Megathrust

Following previous studies (Ramos et al., 2021; Yang, Yao, He, Newman, 2019), we assume that the slip deficit has been continuously accumulated since the CE 1700 earthquake. There are uncertainties associated with this assumption because there are no observational constraints on whether medium-size earthquakes or significant creep occurred in the seismogenic depth range of the megathrust after 1700 but before the instrumental era. Upon interpreting GNSS velocity variations, Materna et al. (2019) proposed temporal variations in megathrust locking in the southernmost Cascadia updip of the Episodic Tremor and Slip (ETS) zone associated with stress perturbations due to offshore M6+ earthquakes in the incoming oceanic plate. We do not include these complicated temporal variations in our calculation of slip deficit because neither the uniqueness of the GNSS data interpretation nor the physical mechanism of the proposed variations is well understood.

With the interseismic locking distribution assumed to be time-independent, the slip deficit s at present (Figures 4a–4c) is given by
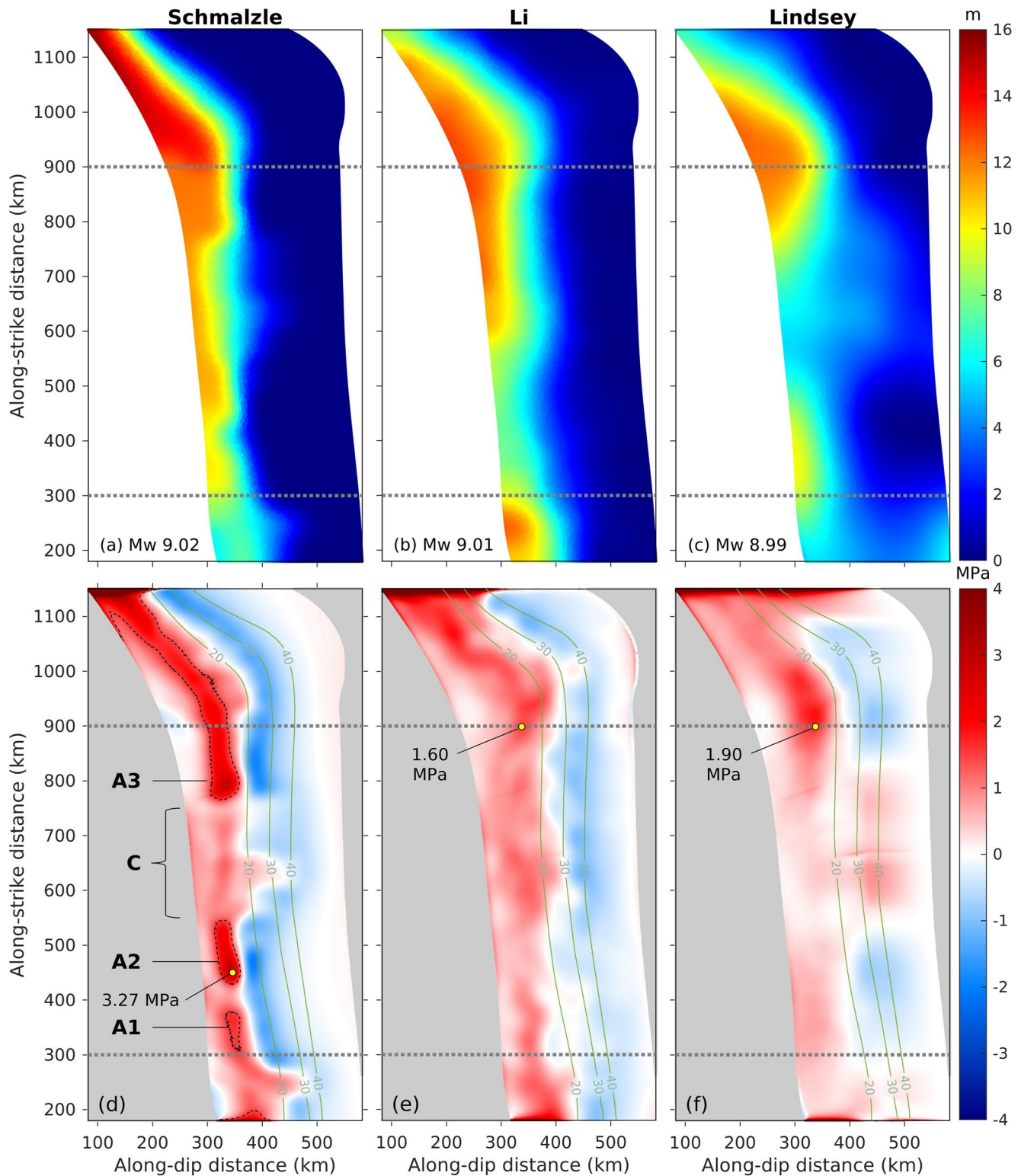
Figure 4. Slip deficit and stress change. (a–c) Total slip deficit with a uniform stress accumulation time of 320 years. Dotted lines: the boundaries of the dynamic simulation domain. (d–f) Dip component of the stress build-up caused by the slip deficit in (a–c). Dotted lines: the boundaries of the dynamic simulation domain. Yellow dots: the point of highest stress change magnitude within the dynamic modeling domain. Dashed lines in (d): 1.5 MPa stress contours. A1, A2, and A3 refer to the stress asperities while C marks the creeping segment extent.

$$s = S_{ann}\phi T_{acc} \tag{1}$$

where S_{ann} is the annual subduction rate, ϕ is the locking ratio, and T_{acc} is the accumulation time which refers to the years since the CE 1700 great earthquake here. As the patch size or node spacing used for each locking model varies, different levels of interpolation are accomplished to the slip deficit. In an elastic model, the incremental stress associated with the accumulation of this slip deficit $\tau(s)$ (Figures 4d–4f) can be readily determined if we treat it as a quasi-static problem where the stress drop is caused by a certain fault slip, and in this case, the complete slip deficit release. Following Yang, Yao, He, Newman (2019) and Ramos et al. (2021), we assume that this incremental stress solely propels the next megathrust rupture (Figure 4) and the initial stress τ_0 is obtained:

$$\tau_0 = \tau(s) + \mu_d \sigma'_n \tag{2}$$

where μ_d is the dynamic friction coefficient and σ'_n is the effective normal stress so the second term refers to the dynamic stress τ_d.

Our assumption implies that the "base level" of the fault stress plays no role, that is, whether the CE 1700 event feature complete or partial stress drop is unimportant. It also means that the spatial heterogeneity of the fault stress distribution just after that earthquake is unimportant. This assumption is obviously a leap of faith, but it is theoretically consistent with the slip-weakening friction law invoked in our modeling which will be explained in Section 3.4, and it makes it operationally possible to derive initial fault stress from interseismic locking models. Note that the rheology of the megathrust is thermally constrained where the critical temperature for earthquakes is around 350°C, corresponding to a downdip seismogenic limit of around 30 km in Cascadia (Flück et al., 1997; Hyndman & Wang, 1995; McCrory et al., 2014). Therefore, the incremental stress derived from one of the locking models shown in Figures 1c and 4c, which occurs far deeper than the commonly assumed seismogenic depth limit in the southernmost and central Cascadia (Figure 4f), is unphysical and probably an inversion artifact. To confine seismic rupture within a reasonable depth range, we use a cosine function to taper the fault stress in this model to zero from 35 to 75 km depth (Figure 4f).

Effective normal stress σ'_n is defined by $\sigma'_n = \sigma_n - P_f$, with σ_n being the normal stress and P_f being the pore fluid pressure. Global subduction zones generally exhibit very high P_f due to geological mechanisms (Saffer and Tobin, 2011), consistent with the low apparent friction constrained by heat flow data (X. Gao & Wang, 2014). A near-lithostatic P_f at ~95% on the Cascadia subduction interface has been supported by the force-balance model (Lamb, 2006) and stress field rotation across the Cascadia megathrust constrained by seismicity (D. Li et al., 2018). Audet et al. (2009) also inferred high Poisson's ratios within the oceanic crust beneath Vancouver Island which suggests near-lithostatic P_f due to the low-permeability plate interface updip of the mantle wedge. For simplicity, we assumed a uniform σ'_n of 50 MPa (i.e., lithostatic P_f) on the entire megathrust regardless of how the shear stress varies along the fault to emphasize the effects of stress build-up. Such lithostatic P_f and constant σ'_n are shown to be possible at elevated pressures in a maturely deformed fault zone (Rice, 1992). Furthermore, 50 MPa is a typical value over the velocity-weakening region which is often used in earthquake simulation studies (Lapusta & Liu, 2009; Michel et al., 2017; Yang, Yao, He, Newman, Weng, 2019). Compared to the case of sub-lithostatic P_f, dynamic simulations using lithostatic P_f may promote peak slip and peak slip rate at shallow depths and demonstrate a lower dependence of stress drop with depth (Madden et al., 2022).

Cascadia is well-known for ETS events (Rogers and Dragert, 2003). X. Gao and Wang (2017) suggest that the effective normal stress in the ETS region is exceptionally low because of near-lithostatic fluid pressure and the ETS zone is rheologically separated from the seismogenic zone, and thus is not involved in dynamic rupture. Furthermore, Ramos and Huang (2019) show that velocity-strengthening frictional behaviors in the transition zone could lead to less downdip coseismic slip and even arrest in the ETS zone. As will be shown in Section 4.2, in our models the rupture is arrested before reaching the ETS zone without additional constraints, which is consistent with the notion of X. Gao and Wang (2017) as well as Ramos and Huang (2019).

Based on findings of high-rate friction experiments (e.g., Di Toro et al., 2011), we set a dynamic friction coefficient of 0.2 (i.e., dynamic stress level of 10 MPa) for the fault below 7 km and assume it to be constant. The southern Cascadia material for the frontal thrust is velocity-weakening while the northern Cascadia material is velocity-strengthening (Stanislowski et al., 2022). For simplicity, we assume that the frontal thrust is neutrally stable by increasing the dynamic coefficient linearly to the static coefficient levels of 0.2656 and 0.2332 for Schmalzle and Li models respectively (Figure 3b and Table 1) from 7 km updip to 5 km depth.

Table 1
Model Parameters in Dynamic Rupture Simulations

Fault parameter	Schmalzle model	Li model
Static friction coefficient, μ_s (τ_s/σ_n')	0.2656	0.2322
Dynamic friction coefficient, μ_d (τ_d/σ_n')	0.2	0.2
Effective normal stress, σ_n' (MPa)	50	50
Critical weakening distance d_c(m)	0.6, 1	0.6, 1

3.4. Fault Frictional Law

The fault is assumed to be governed by the linear slip-weakening law (Ida, 1972) in which fault shear stress τ_f is given by Aagaard et al. (2013a),

$$\tau_f = \begin{cases} \tau_c - \left(\mu_s - (\mu_s - \mu_d)\frac{d}{d_c}\right)\sigma' & d \le d_c \text{ and } \sigma_n' \le 0 \\ \tau_c - \mu_d\sigma' & d > d_c \text{ and } \sigma_n' \le 0 \\ 0 & \sigma_n' > 0 \end{cases} \quad (3)$$

where d_c is the slip-weakening distance, τ_c is the cohesive stress, and d is the slip distance. The fault shear stress (τ_f) decreases linearly with increasing fault slip when $d < d_c$ but stays constant when $d > d_c$. It should be emphasized that, according to the slip-weakening law, the rupture behavior is controlled by the relative ratio between strength drop and initial stress, also known as the relative prestress ratio $R = \frac{(\tau_0 - \mu_d\sigma_n')}{(\mu_s - \mu_d)\sigma_n'}$ (Aochi & Madariaga, 2003; Ulrich et al., 2022; Xu et al., 2015), instead of the absolute stress level.

We set the yield strength τ_s, which is the product of static friction coefficient and effective normal stress, to be uniformly 0.01 MPa above the maximum initial shear stress τ_0^{max} on the fault within the dynamic modeling domain (Figure 3b and Table 1), as shown in Equation 4.

$$\mu_s = \frac{\tau_0^{max} + 0.01 \text{ MPa}}{\sigma_n'} \quad (4)$$

The assumed homogeneity of the yield strength can be understood as an indication of relatively smooth megathrusts that are conducive to very large earthquakes, and its low amplitude reflects the low fault strength as inferred from heat flow data (X. Gao & Wang, 2014). Given the heterogeneous initial stress, this assumed yield strength implies critically prestressed conditions in areas with the highest initial stress, which are possible for initiating earthquakes, while most regions remain under-stressed. This may reconcile with the observed seismic quiescence in Cascadia if the megathrust is operating under low shear stress with efficient dynamic weakening (Lambert et al., 2021). More importantly, although the actual yield strength in the present is unknown, this assumption reflects the future scenario when the megathrust is indeed critically stressed. For instance, if the actual yield strength is approximately homogeneous but higher than the current setting, and the stress continues to accumulate in a similar pattern in the future as suggested by the locking models, the overall rupture extent would still be similar.

The highly compliant, frontal region of the accretionary prism could significantly impact the rupture scenarios as its inelastic deformation can act as an energy sink (Galvez et al., 2014). We tested the sensitivity of the assumed depth limit to the weak frontal prism. We found that strong free-surface reflections and amplified fault slip would be generated to facilitate trench-breaching rupture if a thinner frontal prism was used, but rupture would be arrested if a thicker frontal prism was used (Figure S3 in Supporting Information S1). For simplicity, we adopt an average depth range (i.e., 5–7 km) for the frontal prism according to the velocity model of Stephenson et al. (2017) (Figure S4 in Supporting Information S1). Similar to Ramos et al. (2021), we add cohesion to the segment of the megathrust overlying the assumed frontal prism (Figure 3c) to suppress undesired rupture initiation near the trench.

Due to heterogeneous fault slip with very little or even no slip in some portion of the fault, the critical weakening distance d_c has to be spatially heterogeneous for it to be smaller than the fault slip (Cocco et al., 2009; Dieterich, 1986). The estimates of d_c scatter from 0.1 to 10 m and might drop down to the millimeter scale under different conditions in lab frictional experiments (Di Toro et al., 2011; Kuo et al., 2014). For natural faults, seismic observations possibly scale with local final slip (Chen et al., 2021; Fukuyama & Mikumo, 2007; Mikumo et al., 2003; Viesca and Garagash, 2015) and can potentially correlate with fault roughness and maturity (Marone and Kilgore, 1993; Ohnaka, 2003). The d_c heterogeneity also helps explain the self-similar rupture growth mechanism independent of the final magnitude (Ide & Aochi, 2005). However, constraining d_c on natural faults prior to large events remains challenging due to the lack of sufficient coseismic observation constraints (Weng and Yang, 2018) as well as complex fault zone structures (Chen & Yang, 2020). Moreover, although d_c has been

estimated for previous events (Chen et al., 2021; Kaneko et al., 2017; Mikumo et al., 2003), its heterogeneities and consequent governing effects on earthquake rupture propagation have been seldom reported (Gallovič et al., 2019). As a numerical requirement, we assume a uniform d_c to focus on the heterogeneities from interseismic locking models. Ensuring fair comparison among locking models is another challenge in deciding on d_c because the same d_c represents different fracture energy given the different initial stress and yield strength in each model. Along with the large uncertainties associated with the choice of d_c, we test different uniform d_c values to see how the results are affected. In Section 4.3, we will discuss the results using d_c of 1 and 0.6 m.

3.5. Numerical Resolution

Our models need to meet the resolution requirement for both mesh size and time step. A cohesive zone refers to the fault plane portion behind the crack tip where shear stresses drop from static to dynamic value with a slip less than d_c (Ida, 1972). The cohesive zone of in-plane (mode II) ruptures can be estimated by the following equation (Day et al., 2005)

$$\Lambda = \Lambda_0 A^{-1}(v), \Lambda_0 = \frac{9\pi}{32} \frac{\mu}{1-v} \frac{d_c}{\tau_s - \tau_d}, \tag{5}$$

in which μ is the shear modulus and v is the Poisson's ratio. Considering d_c of 0.6–1 m, the static cohesive zone sizes are around 7.5–25 km. Given a lower bound for shear wave speed V_s of 3.165 km/s and a rupture speed of 3.1 km/s, $A_{III}^{-1} = \left(1 - V_r^2/V_S^2\right)^{1/2} = 0.2$, the dynamic cohesive size can be as small as ~1.5 km. Aagaard et al. (2013b) demonstrate that PyLith can resolve cohesive zones around 1.5 times the size of the tetrahedral elements. Therefore, our element size of 500 m on the fault can resolve cohesive zones in our models.

The choice of mesh size and time step of the dynamic simulation must also follow the Courant-Friedrichs-Lewy (CFL) condition (Courant et al., 1967) to ensure that the numerical scheme is stable and converging to the correct solution:

$$CFL \equiv \frac{|u|\Delta t}{\Delta x} \leq 1, \tag{6}$$

where Δt is the time step, Δx is the mesh size, and u is the velocity, so that the time step is required to be smaller than the time needed for maximum wave speed to propagate across the shortest edge of the mesh element (Aagaard et al., 2013a; Gnedin et al., 2018; Igel, 2017). The highest P-wave velocity prescribed is around 7,600 m/s (Figure 3) and the shortest edge is 500 m, hence the time step must be less than 0.066 s. Accordingly, our dynamic simulations are computed with a timestep of 0.007 s, and the output to fault, surface, and synthetic stations are written every 1, 0.07, and 0.007 s respectively. The duration for each dynamic simulation is 300 s so that the seismic waves propagate out of the dynamic model domain and the fault slip remains constant.

3.6. Rupture Initiation

The nucleation zone refers to the area where the rupture begins. In the prescribed nucleation zone, the initial stress has to meet the yield strength to initiate the rupture. To initiate a rupture, we artificially decrease the yield strength inside the designated nucleation zone by decreasing the static friction coefficient within the nucleation zone from the τ_s values shown in Table 1 to $\tau_s^i = 0.2001$ so it is noted that there is no spontaneous dynamic rupture occurring within the nucleation zone. In order to initiate a spontaneous rupture, a nucleation zone needs to exceed a critical size (Day et al., 2005; Galis et al., 2015; Yang, Yao, He, Newman, Weng, 2019),

$$A_1 = \frac{3\pi^3}{2^{11}} \frac{\overline{\tau_0 - \tau_d}}{\tau_s - \tau_s^i} \frac{(\tau_s - \tau_d)^2}{(\overline{\tau_0 - \tau_d})^4} \mu^2 d_c^2 \tag{7}$$

So $\overline{\tau_0 - \tau_d}$ and $\tau_s - \tau_s^i$ denote average static stress drop and strength decrease within the nucleation zone respectively. Galis et al. (2015) suggest that rupture initiation is mainly determined by the nucleation area while the nucleation shape is less important, hence we adopt circular nucleation zones. For instance, given an average static stress drop of 1.5 MPa and d_c of 0.6 m for the Schmalzle model, the critical area is 585 km², referring to a radius of 13.6 km for a circular nucleation zone, comparable with those adopted in dynamic modeling studies for the
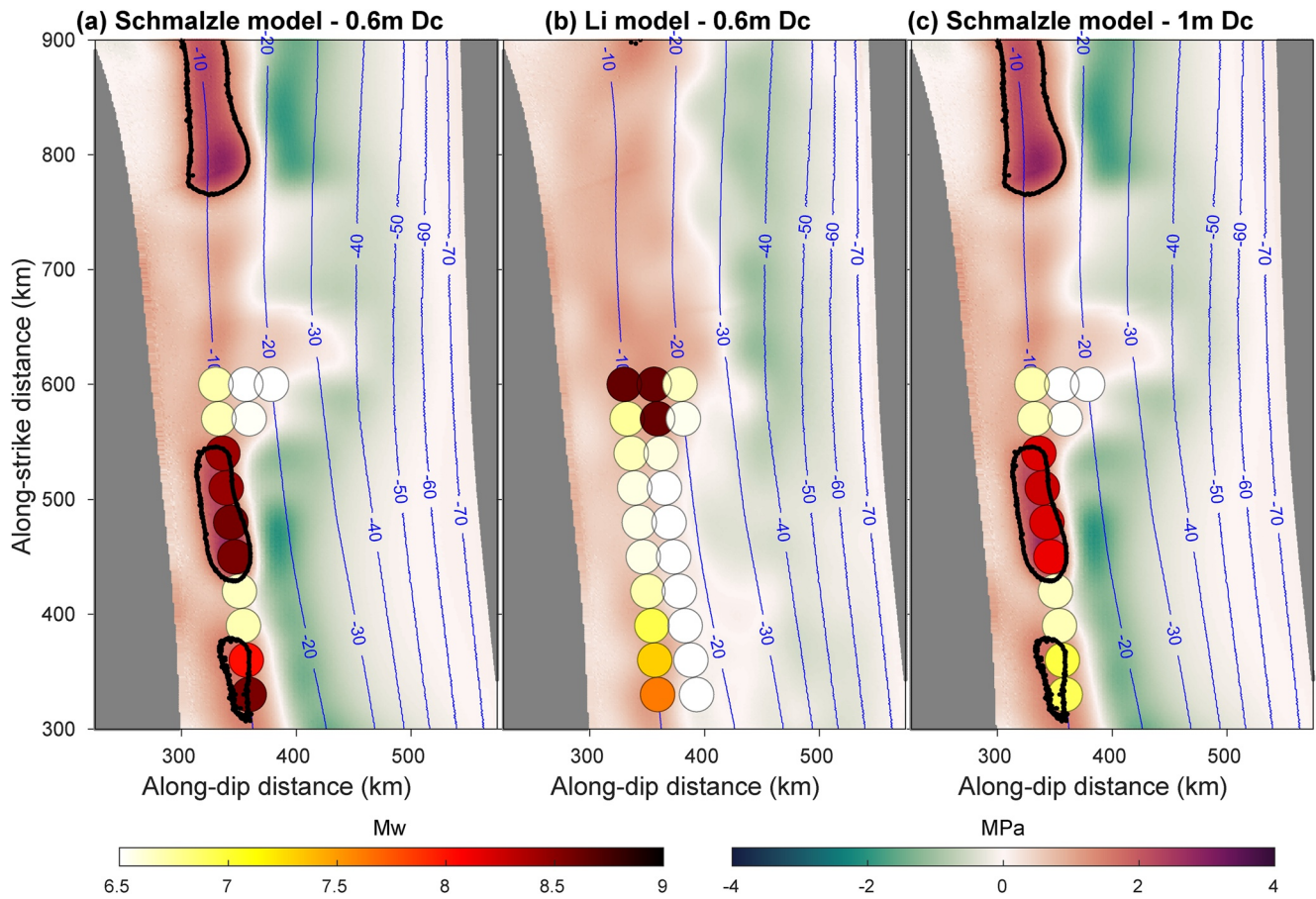
Figure 5. Moment magnitude dependence on hypocenter locations. Map view of the moment magnitudes of rupture scenarios nucleated at each location (circles) with the stress build-up in the background, and slab depth contours (blue lines). (a) Scenarios derived from the Schmalzle model using a dc of 0.6 m. Black lines: 1.5 MPa stress contour, same as in Figure 4. (b) Scenarios acquired from the Li model using a dc of 0.6 m. (c) Same as (a) except for a dc of 1 m (Figure S6 in Supporting Information S1).

2011 M9.0 Tohoku earthquake (Duan, 2012; Galvez et al., 2014; Ide & Aochi, 2013). Although there are existing studies using smaller (e.g., radii of 3–5 km in Yang, Yao, He, Newman, 2019) or hierarchical growing nucleation zones according to stress (e.g., Ramos et al., 2021; Ulrich et al., 2022), we adopt a uniformly large nucleation zone size for the hypocenter locations because the static stress drop in our model is low. In this case, whether the ruptures grow into runaway events solely depends on the stress state inside and near the nucleation sites.

We tested nucleation zone radii of 10 and 15 km. With different nucleation sizes, the model-predicted rupture scenarios for the same hypocenter locations are similar (Figure S5 in Supporting Information S1). To ensure that our rupture scenarios could represent first-order features from the interseismic locking models instead of the interpolation methods, the nucleation zone size has to be comparable to the patch size or node spacing used during inversion, especially for the Li model. Thus, we adopted a larger radius of 15 km. We selected ten along-strike hypocenter locations in southern Cascadia spanning from 41.77° to 44.47° latitude, separated by 30 km in strike and 10 km in depth. Since only positive stress drop inside the nucleation zone can drive the rupture, we conduct simulations with nucleation zones in the area of positive stress change distribution in each locking model (Figure 5).

4. Results

4.1. Stress Build-Up From Locking Distribution

From static calculations as described in Section 3.3, we obtain distributions of stress accumulation from the total slip deficit (Figure 4). Since the stress change along strike is negligibly small, only the dip component is shown

in Figures 4d and 5f. Nevertheless, the strike component is used in our dynamic simulations and the points of the highest stress change are determined by the magnitude of stress change vectors. The slip deficit distributions calculated from the locking models have similar patterns and their moment magnitudes within the static model domain only differ by 0.03 (i.e., M_w 8.99–9.02) (Figure 4). All three locking models feature high slip deficit above 12 m in northern Cascadia (above 900 km along-strike distance in Figure 4). The largest contrast between the models is in the south and central segments. For example, the segment that exhibits more creep is located at 550–750, 300–550, and 500–700 km in the Schmalzle, Li, and Lindsey models, respectively, with different maximum slip deficits (Figure 4a–4c). The derived stress accumulation distributions display a larger difference in along-strike variations among these models (Figure 4d–4f).

The depth extent of positive stress build-up based on the Schmalzle model extends to ∼20 km depth. We can locate three high-stress patches, labeled A1, A2, and A3 in Figure 4d in our dynamic model domain. A2 hosts the maximum stress build-up of 3.3 MPa. Between the A2 and A3, there is a creeping segment with obviously lower stress (labeled C in Figure 4d). Such stark along-strike variations are not that obvious in the slip deficit distribution (Figure 4a), because the stress accumulation is proportional to the second derivative of slip deficit. While A2 and A3 host sharp downdip decrease in slip deficit within a narrow locking zone, the C segment has a more gradual decrease with deeper locking depths. This illustrates that the stress distributions can reveal the seismic potentials that may not be identified as first-order features in slip deficit distributions.

The stress build-up based on the Li model shows a more uniform along-strike distribution, except in the northernmost region where the highest slip deficit takes place (Figure 4). The positive stress in this model extends deeper, to ∼30 km depth. Although it has a longer zone of low slip deficit than in the Schmalzle model, there are no distinct high-stress patches but only a slightly low-stress patch at 400–500 km (Figure 4e). The maximum accumulated stress in the dynamic model domain is only 1.7 MPa.

In the Lindsey model, the stress state is significantly higher in the north than in the south, implying that the south is unlikely to host runaway ruptures if we assume a uniform yield strength. According to Equations 4 and 7, a huge nucleation zone size of more than 20 km radius is required to initiate a spontaneous dynamic rupture, otherwise, simulations from all hypocenters result in self-arrested ruptures (Figure S7 in Supporting Information S1) so the results are not further evaluated in this study. This suggests that the frictional parameters should vary in the north and the south if ruptures initiate from the south, which may be investigated in the future. However, it is noted that the Lindsey model exhibits a somewhat similar along-strike variation of stress distribution to the Schmalzle model, with a low-stress gap at 550–750 km (Figure 4). Therefore, segmented ruptures and high-slip patches could potentially occur in similar locations as the Schmalzle model. On the other hand, the Lindsey model displays a smooth stress distribution akin to the Li model, hence it may be prone to FMR which will be introduced in Section 4.3.

4.2. Predicted Rupture Scenarios

Using the initial stress which includes accumulated stress derived from locking models, we initiate the ruptures with a range of hypocenter locations. In some dynamic scenarios, the ruptures propagate outside with considerable rupture extent, classified as runaway scenarios. The examples of runaway scenarios using d_c of 0.6 and 1 m are shown in Figures 6 and 7 and Figure S6 in Supporting Information S1 respectively. While in other cases, the rupture propagation stops immediately outside the nucleation zones due to the lack of elastic energy release to overcome the fracture energy required to weaken the fault, termed self-arresting events (Figure 5). The moment magnitude for scenarios is calculated according to the integral of the final slip (d) over the fault plane area (A) using an average shear modulus (μ) of 35 Gpa ($M_0 = \mu Ad$; $M_w = 2/3 \times (\log_{10}(M_0) - 9.1)$). Our moment magnitude gives a lower limit for the scenarios that propagate out of the model domain (e.g., Figures 6e and 6g). The slip rate means the relative particle velocity across the fault while the rupture speed is the rate of rupture front movement (Rowe and Griffith, 2015), calculated every 10 s.

We classify the self-arresting and runaway events explicitly. According to the empirical relationships between the rupture area and magnitude, the rupture within the nucleation zone is around M_w 6.5 (Wells and Coppersmith, 1994). Earthquakes generally have rupture velocities higher than 1 km/s (Rowe and Griffith, 2015) and demonstrate a ratio between rupture velocity and v_s starting from around 0.35 (Chounet et al., 2018; Weng and Ampuero, 2020). Since our v_s at trench (5 km depth) is 3.17 km/s, we expect runaway ruptures to reach
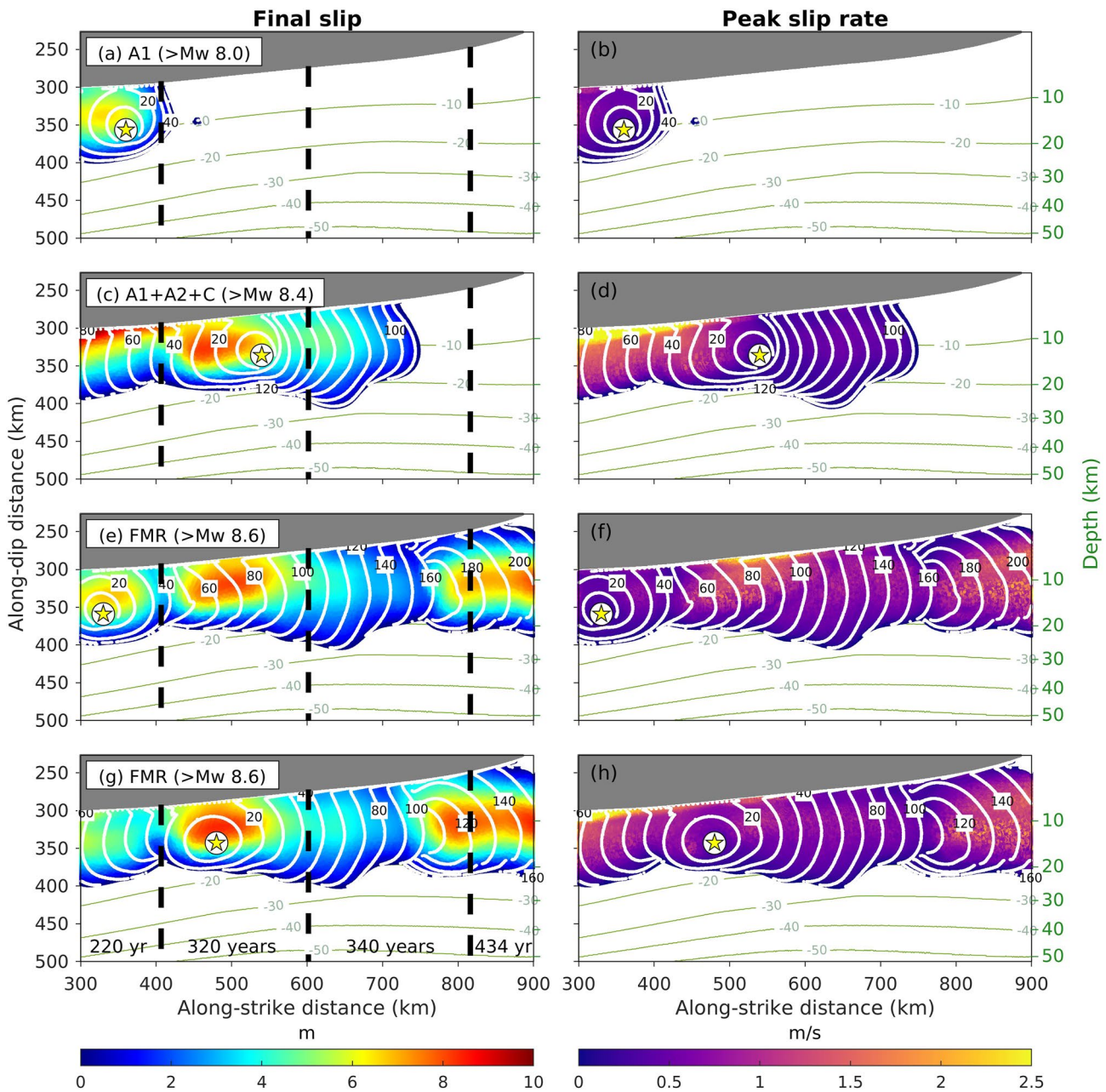
Figure 6. Dynamic rupture scenarios derived from the stress distribution of the Schmalzle model using a dc of 0.6 m. (a, c, e, g) Final slip distribution. Stars: hypocenter locations. Olive-green contours: slab depth contours. Rupture fronts (white contours) are displayed every 10 s and numbered every 20 s. Black dashed lines: recurrence time intervals of 220, 320, 340, and 434 years (Goldfinger et al., 2017) as written in (g). The labeled M_w is calculated by slip within the model domain, thus scenarios with slip extending outside the domain should have larger magnitudes. (b, d, f, h) Peak slip rate throughout the rupture. Stars: hypocenter locations. Olive-green contours: slab depth contours. (a, b) Scenario rupturing the A1 asperity. (c, d) Scenario rupturing A1 and A2 asperities and part of the creeping segment C. (e, f) Full-margin rupture (FMR) initiated from A1. (g, h) FMR initiated from A2.

rupture velocities higher than 1.11 km/s (0.35 v_s). Consequently, we define the scenarios with $M_w < 6.5$ and rupture speed less than 1.11 km/s as self-arresting ruptures and those above as runaway ruptures. Our analysis will only focus on the runaway ruptures, considering self-arresting ruptures are merely the results of artificial nucleation.

We further divide the runaway ruptures into segmented ruptures and FMR. "Full-margin ruptures" represent rupture scenarios that propagate out of the entire model domain. Due to computational limitations, the dynamic model domain does not span the whole megathrust and occupies the region where the locking models differ
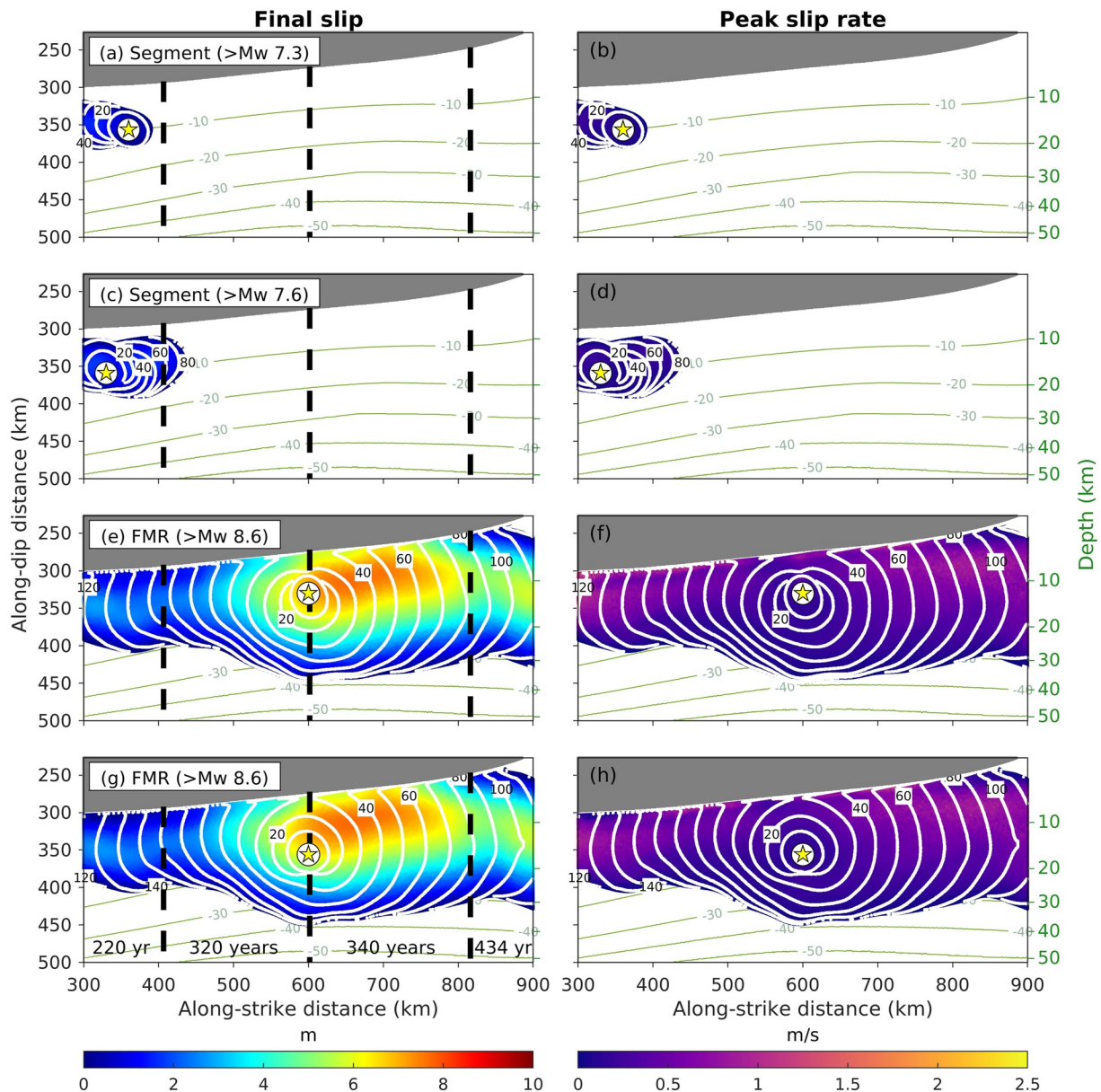
Figure 7. Dynamic rupture scenarios derived from the stress distribution of the Li model using a dc of 0.6 m. Same as Figure 6, except for the Li model. (a–d) Segmented rupture scenarios. (e–h) Full-margin rupture for different hypocenter locations.

most from each other. However, ruptures propagating out of the domain would eventually grow into FMR due to the stress state in the northern and southernmost Cascadia. Since northern Cascadia holds very high stress levels for all locking models (Figures 1 and 4), it is naturally expected that rupture scenarios that break a portion of the northern segment within the dynamic domain would ultimately rupture the entire northern region. Similarly, the southern segment inside the domain has consistent stress levels with the southernmost Cascadia outside of the domain, hence it is very likely to break the southernmost Cascadia as well. Therefore, we name the ruptures propagating out of the south and north of the domain as "full-margin ruptures" in the following context. In contrast, the scenarios where their along-strike rupture extents within the model domain are regarded as segmented ruptures.

FMR are shown in both the Schmalzle-based (Figures 6e–6h) and the Li-based scenarios (Figures 7e–7h) with maximum final slips of 8.5 and 7.3 m respectively. Those of the Schmalzle model are larger than M_w 8.6, reaching a rupture speed of 3.1 km/s and a peak slip rate of 4.5 m/s. The source durations last for more than 150–200 s
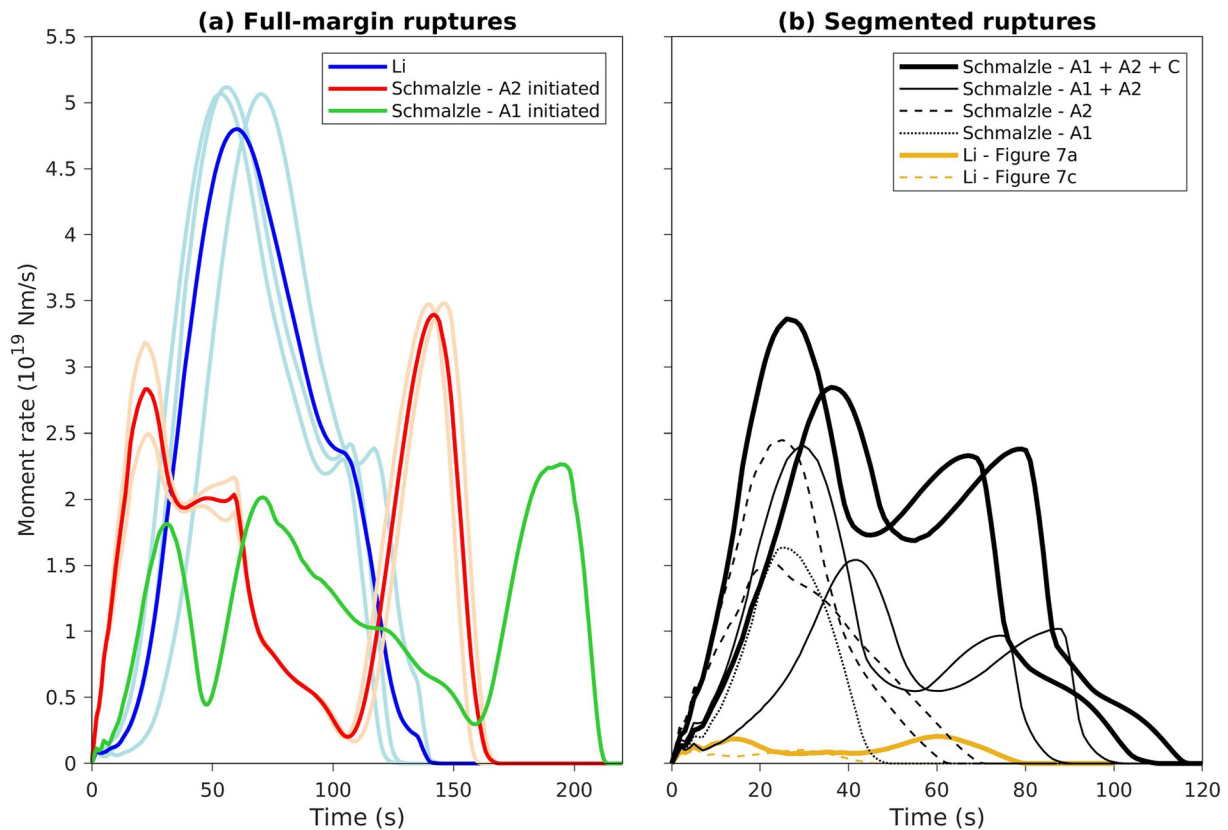
Figure 8. Moment rate functions from dynamic rupture simulations. (a) Moment rate of all full-margin rupture scenarios. Moment rate functions of individual neighboring rupture scenarios are indicated by lighter colors (light blue for the Li model and pink for those initiated from A2 in the Schmalzle model) and the average is marked by solid colors (blue for the Li model and red for the A2 initiation in the Schmalzle model). Note that there is only one event initiated from A2 in the Schmalzle model (green line). (b) Moment rate of all segmented ruptures for the Schmalzle model (black lines) and Li model (orange line). A1 and A1 + A2 + C ruptures were derived using a dc of 0.6 m while A2 and A1 + A2 scenarios were simulated with a dc of 1 m (Figure S6 in Supporting Information S1). The only segmented event from the Li model utilizes a dc of 0.6 m.

depending on the hypocenter location (Figure 8a). On the other hand, the moment magnitudes of FMR from the Li model are also higher than M_w 8.6. They have a slightly lower rupture velocity of 2.8 km/s and a peak slip rate of 2.7 m/s. The source duration is around 140 s (Figure 8a). The FMR of the Schmalzle model and the Li model arrested at 30 and 40 km depths respectively. All are initially predominated by crack-like ruptures, evolving into pulse-like ruptures (Movies S1–S4).

Despite having the same accretionary wedge setting as in Figure S4b in Supporting Information S1, all the scenarios shown here, except case 6c, do not demonstrate the large near-trench slip as tested above because of the different hypocenter locations and stress distribution. For the Schmalzle model, as the rupture initiates in the south, the combined effects from rupture directivity and free surface reflection in the south are smaller as compared to initiation from the north. As for the case of 6c, its hypocenter is located further north, thus allowing a stronger directivity. However, such high slip trench features are also absent in the north even with hypocenters in the south. This is because while the rupture propagates through the central creeping segment, the energy depletes and it is insufficient to cause a large slip until it reaches the high-stress asperity at the north. For the Li model, the high-slip trench is also absent because there are no particular high-stress asperities that could trigger a larger slip near the trench.

Rupture segmentation is observed in both models. From the Schmalzle model dynamic scenarios, we observed one scenario breaking A1 (Figure 6a) and two scenarios rupturing A1, A2, and partly C (Figure 6c). The A1 segmented rupture (Figure 6a) is initiated by a hypocenter location at A1 asperity and the source duration continues for 40 s (Figure 8b), with rupture stopped above 20 km depth. Both A1 + A2 + C scenarios (Figure 6c) are triggered by nucleation at A2 asperity, and the source durations last for 110–120 s (Figure 8b), having slip above

30 km depth. For the Li model, only two dynamic segmented scenarios are found rupturing the southernmost segment. The smaller segmented rupture (Figure 7a) propagates out of the south unilaterally so the observed duration only lasts for 40 s. For the larger segmented rupture (Figure 7c), the rupture initiation is close to the domain boundary and the rupture breaks the south quickly after nucleation while slowly propagating to the north and being arrested above 20 km depth without reaching the trench, resulting in a duration time as long as 80 s (Figure 8b). Except for the A1 + A2 + C dynamic models which have similar rupture evolution behaviors to the FMR (Movie S5), the short segment ruptures (Figures 6a, 7a, and 7c) are primarily crack-like ruptures as the rupture duration is insufficient for them to grow into pulses (Movies S6–S8).

### 4.3. Hypocentral Effects on the Potential Moment Magnitude and Ground Surface Response

In view of the different resulting scenarios, we investigate the effect of different hypocenters in both models with a d_c of 0.6 m. For the heterogeneous Schmalzle model, there is a strong along-strike variation in moment magnitude with respect to the stress distribution (Figure 5a). The nucleation zones within the highest stress patch A2 result in scenarios with $M_w > 8.4$–8.6 and the events within A1 have $M_w > 8.0$–8.6. All the nucleation centers lying outside of the stress asperity result in self-arresting ruptures. This demonstrates the hypocentral dependency of magnitudes in the Schmalzle model.

Meanwhile, the Li geodetic locking model gives a smoother and more homogeneous stress distribution within the model domain that does not flavor rupture segmentation except in the southernmost region where the initial stress is slightly higher (Figure 5b). Although FMR take place with hypocenters in a particular region, it by no means suggests that the ruptures are larger on that site but only shows that the initiation of FMR is sensitive to slight stress perturbations on the fault in our models. This highlights the importance of exploring a range of complexities, such as temporal changes in stress accumulation, background stress level from paleoseismic earthquakes, and heterogeneous frictional properties, in addition to our simplified assumptions because the stress distribution of the Li model has limited constraints on the hypocenter locations favoring large earthquakes.

Apart from the moment magnitude, the hypocentral effects on ground surface response are also noticeable from the synthetic stations (Figure 9a). One limitation of Galerkin finite element methods is numerical wave dispersion, depending on parameters such as the element size, element type, and time integration scheme (Semblat et al., 2011). Despite unstructured mesh and numerical error increasing with propagation distances (Semblat and Brioist, 2000), the resolved frequency ranges show no remarkable variations among the stations in our simulations (Figure S8 in Supporting Information S1). The effective high-frequency cutoff beyond which the spectral amplitude decreases steeply is approximately 0.2–0.4 Hz and the complete cutoff frequency above which there is no propagation (Ihlenburg & Babuška, 1995) is about 1 Hz for all synthetic stations (Figure S8 in Supporting Information S1). The sampling rate every 0.007 s gives a Nyquist frequency of approximately 71 Hz, which is much higher than the complete cutoff frequency limited by the element size. This resolved frequency range is crucial to tsunami generation and partially contributes to engineering purposes (Wirth et al., 2018; Zhang et al., 2010).

We compare the relative velocity magnitude, the square root of the three-component sum of squares of the velocity time series, of synthetic stations near major cities derived from the margin-wide scenarios in both models (Figure 9). Because the ground motions are an approximation without the application of the 3D velocity model, the amplification from sedimentary basins is not considered. Although the rupture extent from the scenarios of different hypocenters in each model is highly similar (Figure 9a), the amplitude of peak ground velocity (PGV) can differ by a factor of two. One outstanding example of the forward rupture directivity effects from different along-strike hypocentral locations comes from the Schmalzle model as hypocenters in both A1 and A2 can generate margin-wide ruptures. Since the rupture front from A1 hypocenter event propagates from the southernmost region to the north of the domain aligning with the direction of slip, the energy piles up from successive fault segments and causes a distinct pulse in the direction of rupture as compared to the A2 hypocenter events. For example, the LOKI station has a PGV of 2.5–3 cm/s for the A2 hypocenters but 6.4 cm/s for the A1 hypocenter (Figure 9ei).

On the other hand, the influence from different along-dip hypocentral locations is subtle in our model because of the small difference in distance, which corresponds to a similar location relative to fault slip. This implies that the difference in synthetic waveforms mostly reflects the regional fault slip evolution. For instance, in the Li
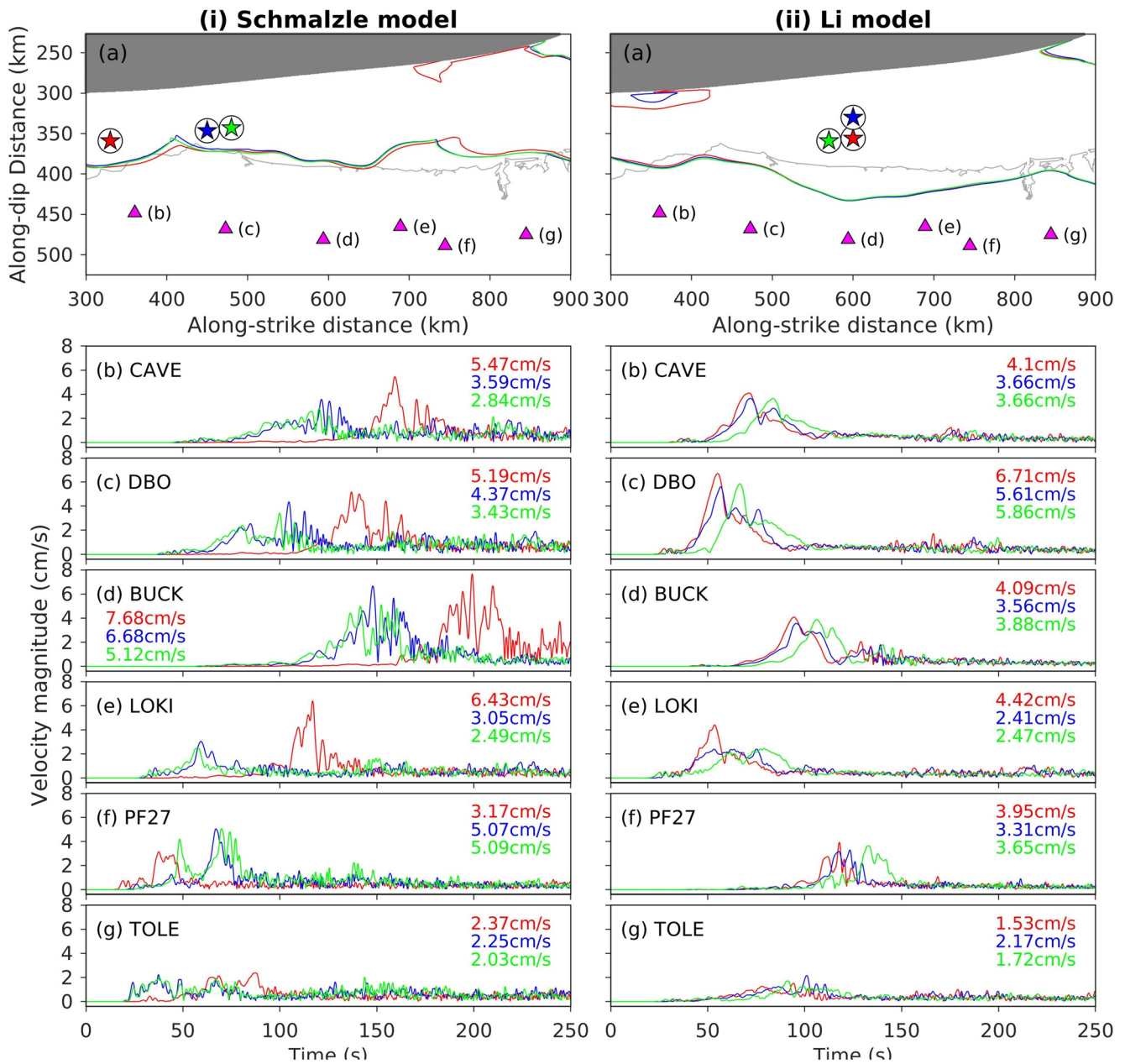
Figure 9. Synthetic velocity magnitude at stations for Full-margin rupture. (a) The 1 m final slip contour of rupture scenarios with the coastline (light gray). The colors of the slip contours match with the star (hypocenter location) colors. Magenta triangles: station locations. Labels beside stations: the plot number. The stations near major cities along the strike are selected from the Pacific Northwest Seismic Network. (b–g) Comparison of velocity magnitudes (three-component combined) among the rupture scenarios in (a) with matching colors. The corresponding peak velocity magnitudes and station names are marked on each trace. (i) Schmalzle model. (ii) Li model.

model, the two hypocenters have the same along-strike distance but different downdip depths—10 and 15 km. The deeper nucleation event (15 km) in red demonstrates slightly larger peak ground velocities than the shallower one (10 km) in blue at stations DBO and LOKI. For the 15 km event, the rupture propagates updip since initiation, setting off a strong wavefront (Figure 7c). However, the 10 km event starts by propagating downdip and is followed by an updip fault slip along the sides of the nucleation zone, creating two wavefronts shortly after the nucleation (Figure 7e). The interference of these seismic waves and those from downdip fault slip leads to a more ambiguous waveform slightly lagging behind the 15 km event even though the 10 km one is in closer proximity to the surface. This suggests that the along-strike rupture directivity primarily controls the tsunami

height and arrival times for the elongated Cascadia megathrust, as opposed to the concentrated locked patch in the Nicoya Peninsula subduction megathrust where along-dip rupture directivity plays a major role (Yang, Yao, He, Newman, 2019).

The effects from hypocenter locations are more prominent and representative in a broader sense as we correlate the surface deformation on the continental block with the distance from rupture in reference to empirical ground motion prediction models (GMPMs) (Figure 10). Specifically, we utilize the GMPMs from Montalva et al. (2022) based on the Chilean subduction zone for PGV and Goldberg et al. (2021) based on global data for peak ground displacement (PGD). The PGV GMPM model includes factors from magnitude, path effect, inslab/interface events, and site effects but the site effects are neglected here. For interface events, the source-to-site distance is described by the shortest distance to the rupture plane R_{rup} which defined as the region exceeding 1 m slip in our study following the approach from S. Yao and Yang (2023), consistent with the contour in Figure 9. For the PGD model, we also ignore the site effect and adopt a simple scaling relation between PGD, M_w, and the generalized mean rupture distance R_{eff} given by

$$R_{eff} = \left(\sum_{i=1}^{n} w_i R_i^p \right)^{\frac{1}{p}}, \quad w_i = slip_i / \left(\sum_{j}^{n} slip_j \right) \tag{8}$$

where n is the number of subfaults, w_i is the weight of subfault based on the fault slip, R_i is the distance to the subfault, and p is the power of the mean. Here we use $p = -4.5$ from the observed earthquake data set (Goldberg et al., 2021). To compare the synthetic ground motions from dynamic rupture simulations with the GMPMs, we calculate the ground-motion residuals by the following equation (Baumann & Dalguer, 2014)

$$residual = \log_{10}(syn) - \log_{10}(pre), \tag{9}$$

in which "syn" is the mean of synthetic PGD or PGV from our simulation and "pre" is the predicted ground motion from GMPMs.

For both PGD and PGV, we sample the results every 5 km with respect to R_{eff} and R_{rup} respectively. The amplitudes and decay trends of our dynamic simulations are generally consistent with the GMPMs in first order (Figures 10e and 10f), indicating that the rupture scenarios are valid for predicting earthquake ground motion (Shi and Day, 2013). However, the decay trends differ in detail due to the contribution of heterogeneous source models, as reported in other physics-based ground motion simulations (Xin and Zhang, 2021; S. Yao and Yang, 2023). For instance, our synthetics clearly show the saturation in PGD amplitude within 30 km which is absent in the GMPM model (Figures 10a and 10b).

We here examine the contribution of hypocenter-dependent effect on ground motion intensity. While PGD reflects the ground shaking intensity at low frequencies, PGV is more sensitive to intermediate frequencies as well as the effects from source parameters (Baumann & Dalguer, 2014; Goldberg et al., 2021; S. Yao and Yang, 2023), hence we shall focus on PGV for the following discussion. Matching with the synthetic waveforms, the hypocentral locations in the Li model here show similar ground shaking with each other due to their proximity (Figure 10d). The difference in PGV among the hypocenter locations is constrained in near-field (<30 km) by a factor of approximately 0.3 (Figure 10d). As the variation is caused by localized fault slip, the effects are most concentrated close to the source. On the other hand, the rupture scenario with the southernmost hypocenter in the Schmalzle model produces remarkably larger PGV than those from the A2 hypocenters by a factor of ∼0.3–0.5 across all distances >30 km while the amplitude difference is similar within in near-field around a factor of 0.1 (Figure 10c). This increasing trend in factor difference with source-to-site distance agrees with forward rupture directivity effects which are expected to be the most concentrated away from the hypocenter (Somerville et al., 1997). This demonstrates that the unilateral rupture from the southernmost hypocentral location results in stronger ground shaking in the on-land seismic stations compared to those bilateral ruptures from the A2 hypocenters.

4.4. Seafloor Deformation and Coastal Subsidence in Margin-Wide Scenarios

We also evaluate the surface deformation patterns for our margin-wide rupture scenarios. PGD of both Schmalzle-based and Li-based scenarios generally lie within one standard deviations predicted by the GMPM,
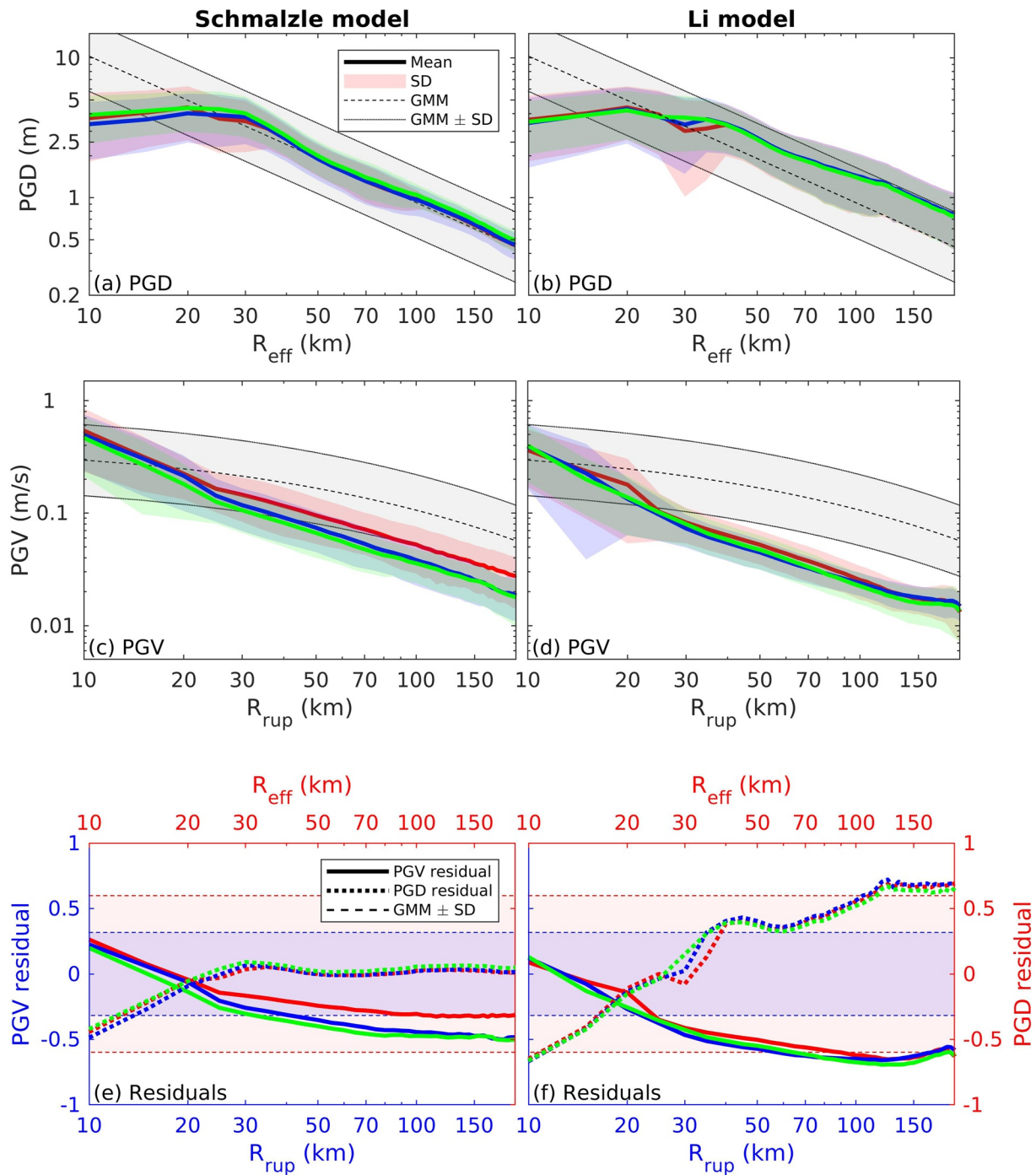
Figure 10. Ground motion variability for different hypocentral locations resulting in full-margin ruptures. (a, b) Peak ground displacement (PGD) as a function of the generalized mean rupture distance R_{eff}. The solid lines are the mean PGD for each dynamic rupture simulation, the colors denote the hypocenters in Figure 9, and the shaded regions are the standard deviations (SD) for the corresponding scenarios. The PGD ground motion prediction model (GMPM) (Goldberg et al., 2021) and its SD are represented by the black dashed line and dotted lines respectively and the areas between one SD are shaded in gray. (c, d): Peak ground velocity (PGV) as a function of the closest distance to the rupture plane R_{rup}. Same plotting as described in (a, b) except for the solid lines indicating mean PGV and PGV GMPM from Montalva et al. (2022). (e, f) The ground motion residuals as a function of source-to-site distances. The PGV and PGD residuals are indicated by solid and dotted lines respectively. The axes of the PGV residual are marked in blue while the PGD axes are shown in red. The SD of the GMPMs and the region within one SD are represented by the dashed lines and the shaded areas corresponding to the axes' colors.
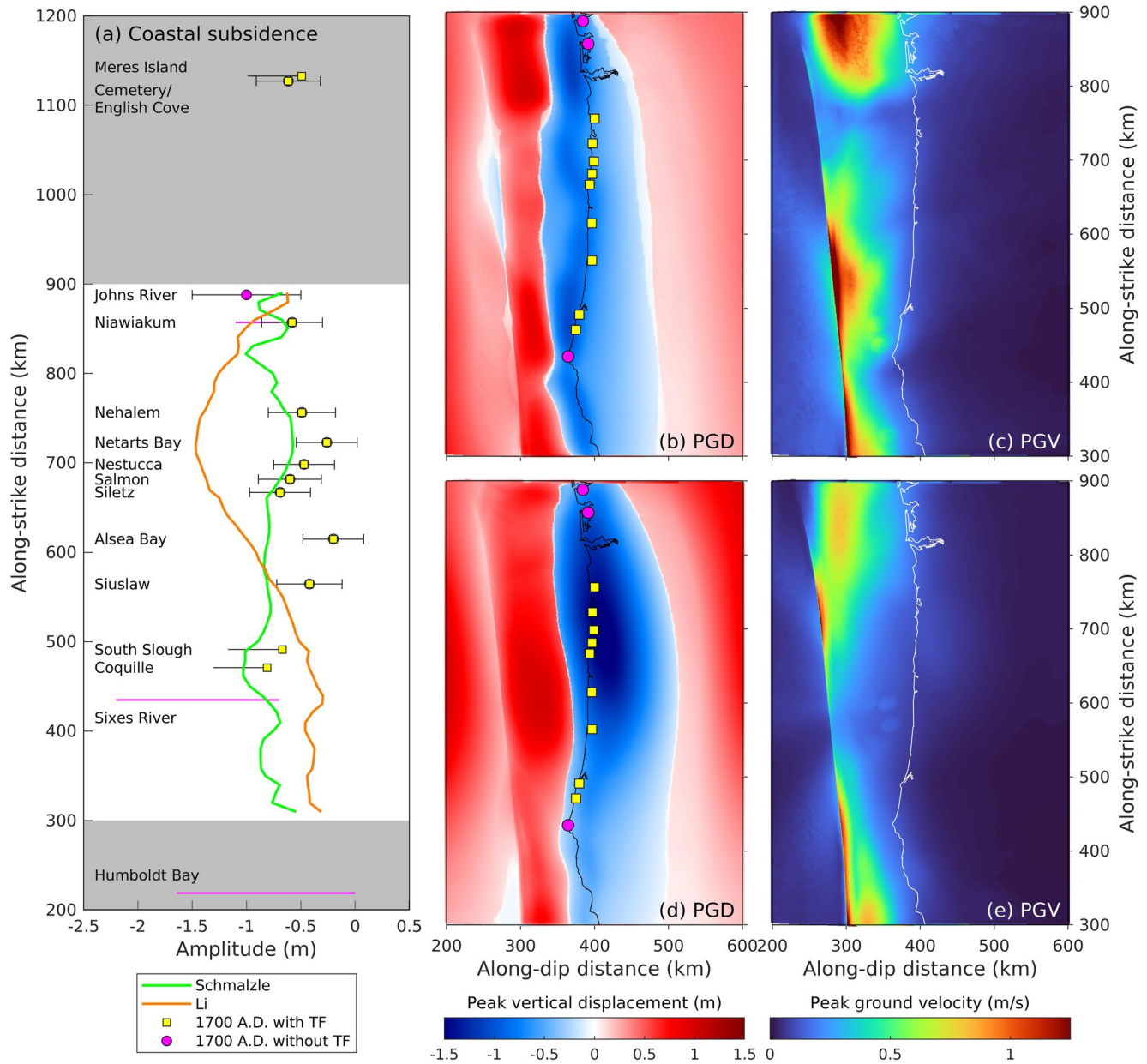
Figure 11. Ground motion intensities of full-margin ruptures (FMR). (a) Average peak vertical ground displacement along the coastline for the Schmalzle model (green line) and the Li model (orange line). Yellow squares: observations sites with transfer function analysis (TF). Pink circles: sites without TF. Error bars: one standard deviation. Black lines with yellow squares at one end: yellow squares as the minimum estimates. Pink line: uniform distribution. Gray patches: regions outside of the model domain. (b) Peak vertical ground displacement of FMR in the Schmalzle model with the coastline (black line). Observation sites with (yellow square) and without (pink circles) TF analysis (P. L. Wang et al., 2013). (c) Average peak ground velocity of FMR derived in the Schmalzle model with the coastline (white line). (d, e) Same as (b, c) respectively except for the Li model.

except for smaller displacement in near-field (<20 km) (Figures 10a and 10b) where the GMPM has limited observations (Goldberg et al., 2021). Compared to the Schmalzle-based scenarios, the Li-based scenarios result in a higher PGD at farther distances due to the larger downdip rupture extent. In the following context, we focus on the vertical component since it primarily controls coastal subsidence and tsunami generation. The peak vertical ground displacements for the Schmalzle-based and Li-based scenarios are similar in magnitude, ranging from −1.1 to +1.0 m and from −1.6 to +1.0 m respectively (Figures 11b and 11d). On the other hand, the maximum PGV of the Schmalzle-based scenarios (i.e., 2.3 m/s) is remarkably higher than that of the Li-based scenarios

(i.e., 1.5 m/s) by half (Figures 11c and 11e). Both models show the highest PGV toward the tip of the continental crust and the northernmost region of the domain.

Coseismic hingeline refers to the point where there is zero seafloor vertical displacement. Compared to the Schmalzle model (Figure 11b), the coseismic hingeline for the Li model (Figure 11d) is further inland, especially for the central and northern segments because the downdip rupture extent of these regions in the Li's model is deeper (Ramos et al., 2021). However, it is noted that the down-dip locking depth of the seismogenic zone is poorly constrained by geodetic data (K. Wang and Tréhu, 2016), thus we only examine the along-strike variations of coastal subsidence instead of the absolute amplitudes.

The average coastal subsidence is then extracted from the peak vertical ground displacement of the data points closest to the coastline in all the margin-wide scenarios in both models (Figure 11a). We then compare the synthetics with the subsidence records of the CE 1700 M9 earthquake. In our scenarios, Li's coastal subsidence gives a significantly longer wavelength along-strike variations compared to the observations with the largest amount of deformation at the high slip patch in the north and decreasing further away. This displacement pattern is similar to that caused by a smooth slip model without high dynamic stress-drop subevents in Wirth and Frankel (2019). For scenarios from the Schmalzle model, the along-strike coseismic subsidence appears to fluctuate with slightly larger deformation in high-slip segments region. The subsidence records of the CE 1700 M9 rupture also exhibit heterogeneous along-strike patterns, which can be matched by models with several high slip patches (P. L. Wang et al., 2013). In our case, the scenarios from the Schmalzle model can reproduce a similar along-strike variation with the observations, mainly due to the higher slip heterogeneity with three high-slip patches (Figure 6) compared to those from the Li model (Figure 7).

5. Discussions

5.1. Potential Rupture Patterns in Correlation With Recorded Segmentation and Recurrence Intervals

The rupture extents of segmented scenarios in the Schmalzle model appear to coincide with the recorded segmentation of paleoearthquakes (Goldfinger et al., 2012, 2017). The A1 scenario was arrested around the 220–320 years recurrence interval boundary (Figure 6a), and all cases for A2 and A1 + A2 ruptures stopped around the 320–340 years boundary as it enters the creeping segment (Figure S6 in Supporting Information S1). The segmented scenarios from the Li model (Figures 7a–7d) also share similar rupture extents with the A1 scenario from the Schmalzle model.

We also find that the margin-wide ruptures can be derived for all models given certain frictional parameters. Given the 320 years of silence and the recurrence intervals of 220–340 years in the south, all segmented scenarios are possible in the current stage. Although there are few constraints on the frictional parameters of the Cascadia megathrust, our combination of parameters allows variations in rupture scenarios, including segmented and margin-wide ruptures comparable with the geological records. This may suggest that the ratio between the frictional parameters and initial stresses is reasonable, if not the absolute amplitudes. The margin-wide rupture initiates at A1 and A2 in the Schmalzle model and the boundary between 320 and 340 recurrence intervals for the Li model. This reflects that at the current state, the possibility of ruptures initiating from the south or central Cascadia growing into a margin-wide rupture cannot be eliminated.

The diverse segmentation in our scenarios results from heterogeneous locking and various hypocenter locations. Ramos et al. (2021) initiated dynamic rupture simulations at locations of highest stress drop in the south, resulting in FMR for scenarios with uniform stress accumulation time, and both full-margin and segmented rupture scenarios using heterogeneous stress accumulation time along strike which is determined empirically. Indeed, the uncertainties in the stress accumulation history could be introduced by a heterogeneous time interval. However, with strong along-strike differences in accumulation time, the stress distribution becomes largely affected by the empirical time interval instead of the locking distribution. Our study shows that segmented ruptures are possible even using a uniform stress accumulation time when different nucleation zones are used. The application of hypocenter locations discovers the possibilities of rupture initiation from a range of stress drops, thus more segmentation patterns are found apart from the largest possible margin-wide ruptures (Figure 12).

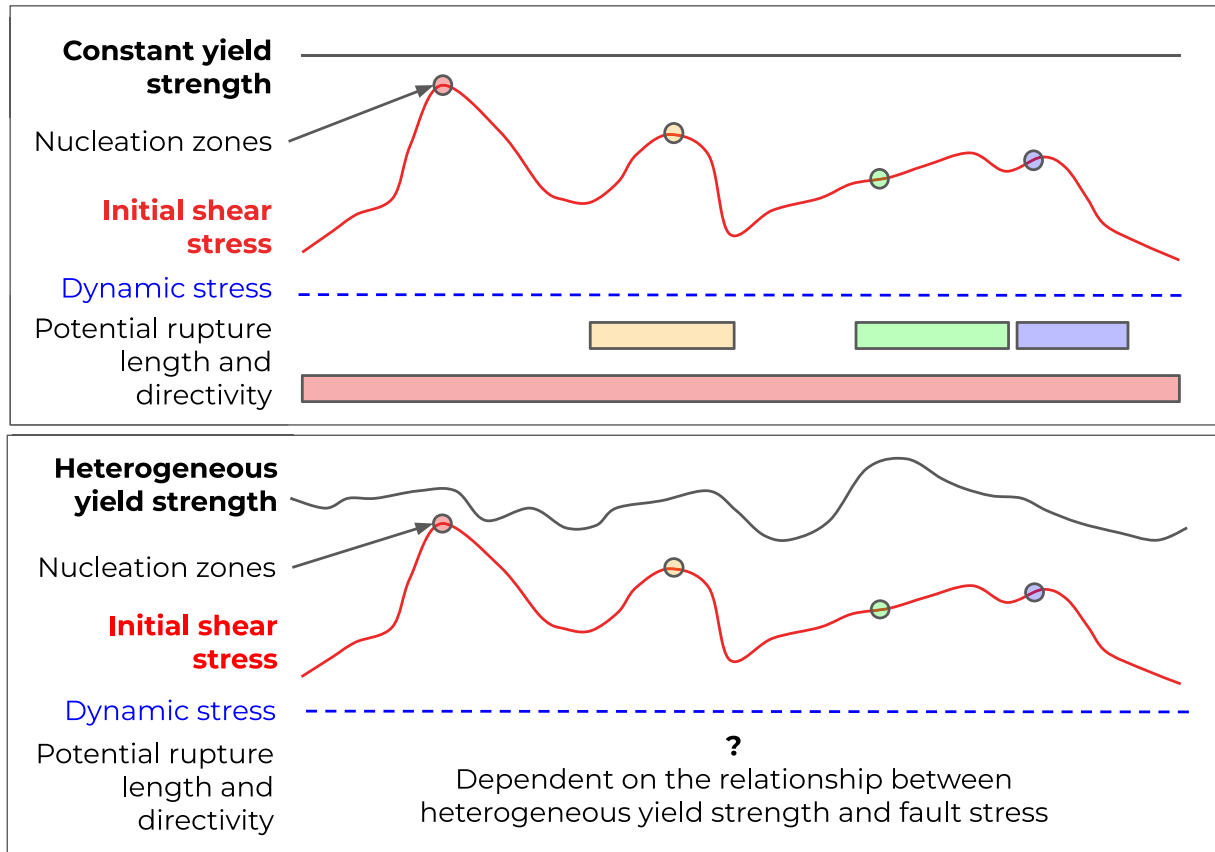## Schematic Diagrams for the effects of nucleation zone location

Figure 12. A schematic diagram demonstrating the potential rupture segmentation by applying different hypocenter locations.

5.2. Simulated Coseismic Subsidence Compared With CE 1700 Records

Although the along-strike variation of the heterogeneous Schmalzle-based coastal subsidence has a reasonable consistency with the paleoseismic records, our synthetic subsidence is generally slightly larger than the observations, exceeding one standard deviation in two sites—Alsea Bay and Siuslaw at the central segment (P. L. Wang et al., 2013) similar to the earthquake sequence simulations (D. Li & Liu, 2021). As for the Li-based scenarios, the coastal subsidence exhibits a much smoother large-scale pattern than the along-strike fluctuations in observations. Here we will provide possible reasons to account for the discrepancies between scenario results and paleoseismic records.

One critical assumption in our research is the homogenous background stress levels immediately after the CE 1700 margin-wide rupture. The true background stress for CE 1700 could in fact be heterogeneous due to the spatial and temporal uncertainties in the geodetic locking and the slip history before the CE 1700 rupture. It is possible to reconstruct best-fit subsidence results by adjusting accumulation time empirically as in Ramos et al. (2021) but this is beyond the scope of our study. Another important factor controlling subsidence is the inelastic accretionary prism deformation. One outstanding example is the 2011 Tohoku-Oki earthquake where the region of the largest slip does not cause the largest tsunami height possibly due to the inelastic deformation of the accretionary prism (Fujiwara et al., 2017; Wilson and Ma, 2021). Han et al. (2017) observed an along-strike variation for the consolidation state of the accreted sediments in Cascadia and propose that this could contribute to the megathrust slip behavior. For instance, offshore Washington has over-consolidated sediments incorporated into the mechanically strong outer wedge, and very little sediment is being subducted, flavoring potential near-trench rupture. On the other hand, a thick sequence of under-consolidated fluid-rich sediment is subducting offshore Central Oregon, possibly facilitating elevated pore pressure, thus promoting possible aseismic slip in this area.
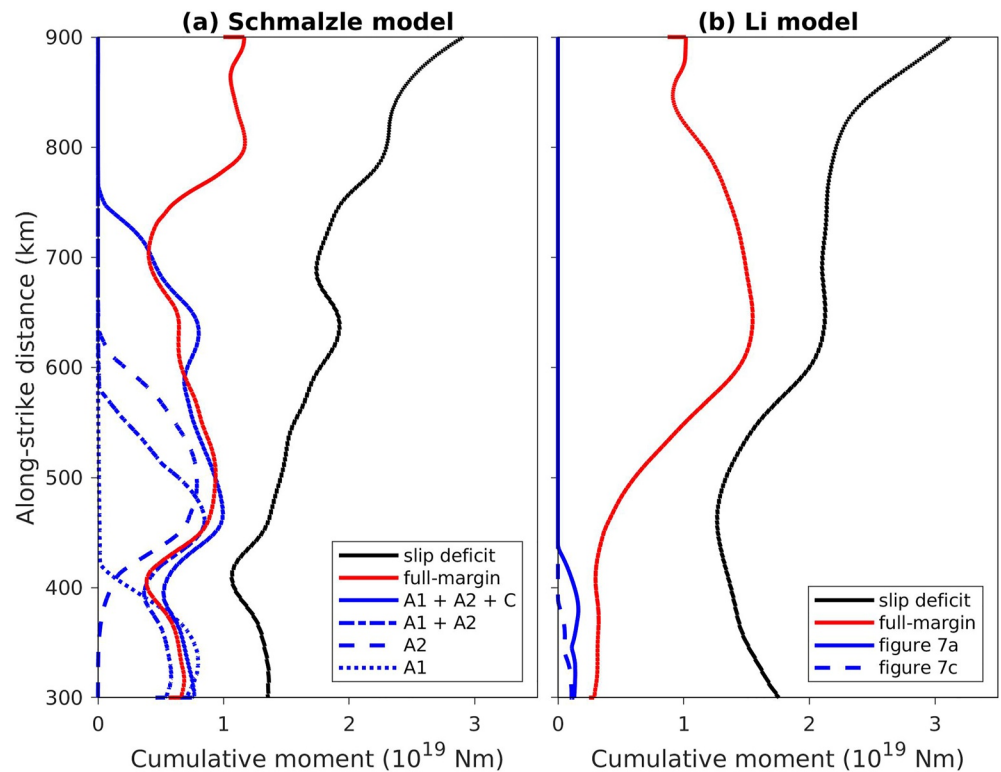
Figure 13. Cumulative moment versus the along-strike distance. The cumulative moment is the product of rigidity, slip, and area, integrated over every 500 m width along strike. Blue lines: average cumulative moment for the segmented scenarios. Red lines: average cumulative moment for full-margin ruptures. Black lines: cumulative moment assuming all slip deficit in Figure 4 are released, also known as the moment deficit (Maurer et al., 2017). (a) Dominant dynamic rupture scenario types and slip deficit for the Schmalzle model. (b) Same as (a) except for the Li model.

Apart from the large coseismic slip patches and shallow accretionary prism, the deeper portion of the megathrust can also greatly contribute to surface deformation even with low to moderate slip if they produce high-frequency seismic radiation (>1 Hz). This high-frequency radiation source at depth was widely observed in megathrust earthquakes (Ye et al., 2016) with remarkable examples including the 2004 M9.2 Sumatra-Andaman, 2010 M8.8 Chile, and 2011 M9.0 Tohoku-Oki great earthquakes (e.g., Lay et al., 2012; Simons et al., 2011; H. Yao et al., 2013). Although high pre-seismic shear stress and frictional heterogeneities have been proposed to contribute to the high-frequency radiating slip patches (Lay et al., 2012; Michel et al., 2017), the physical properties controlling the along-strike location of these subevents remain unclear (Wirth and Frankel, 2019). Should these high-frequency subevents occur, surface deformations of shorter wavelength variations could be generated despite a homogeneous slip distribution like the Li-based scenarios. In particular, Wirth and Frankel (2019) demonstrated the possibility to match the along-strike variations in coastal subsidence of the CE 1700 Cascadia event by prescribing high-dynamic stress-drop subevents along the megathrust. Hence, these factors may account for the deviation of our model subsidence from the data.

5.3. Comparison Between Dynamic Simulations and Static Methods

Our dynamic simulation showcases a lower moment release in all rupture scenarios than estimations from variant static methods. Static methods commonly provide the upper bound of possible slip by assuming a complete release of slip deficit in future earthquakes (Figure 13). The maximum slip deficits within the model domain for both models only differ slightly—12.9 m for the Schmalzle model and 13.0 m for the Li model. Consequently, the maximum slip in the Schmalzle-based dynamic rupture model (8.5 m) contributes about 66% of the maximum slip deficit, and that of the Li model (7.3 m) is about 56%. This difference with the static locking models is observed in a number of studies, including the potential rupture segmentations for the Anninghe fault in west
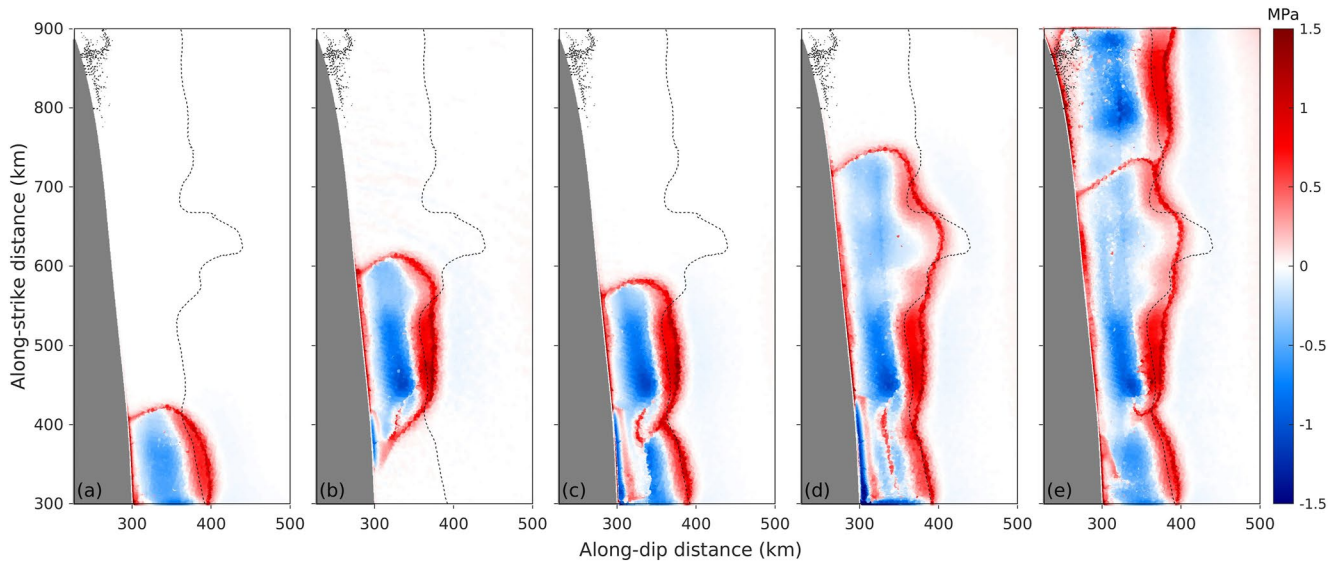
Figure 14. Stress change distributions for the Schmalzle-based rupture scenarios. Dashed lines: contours of zero stress change derived from locking models (Figure 4). The up-dip portion of the contour contains positive stress build-up. (a) Example of A1 rupture (Figure 6a). (b) Example of A2 rupture (Figure S6c in Supporting Information S1). (c) Example of A1 + A2 rupture (Figure S6e in Supporting Information S1). (d) Example of A1 + A2 + C rupture (Figure 6c). (e) Example of a full-margin rupture (Figure 6g).

China (S. Yao and Yang, 2022), the central American subduction zone where the 2012 Nicoya M_w 7.6 earthquake occurred (Yang, Yao, He, Newman, Weng, 2019), Himalaya front where the 2015 Nepal M_w 7.8 earthquake took place (Y. Li et al., 2016), as well as the south American subduction zone where the 2010 Maule M_w 8.8 earthquake occurred (Moreno et al., 2010).
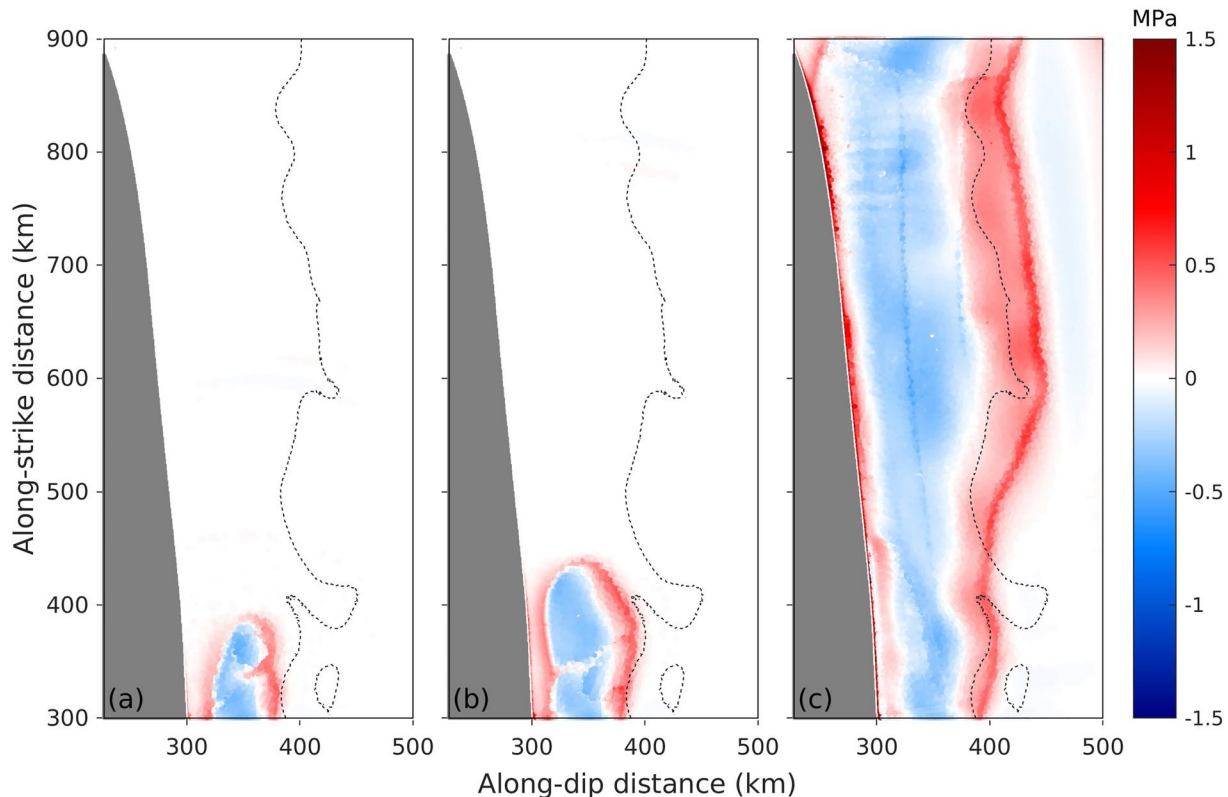
Figure 15. Stress change distributions for the Li-based rupture scenarios. (a) Segmented rupture shown in Figure 7a. (b) Segmented rupture shown in Figure 7c. (c) Average of the full-margin rupture scenarios.

These suggest that given our current frictional parameters, a considerable fraction of the slip deficit in regions of low to moderate stress drop is not released during dynamic simulations in our models (Figures 14 and 15). The stresses on these areas can be relieved later possibly in the form of coseismic events and slow slip events. For instance, Cascadia is well-known for its episodic tremor and slow slip events. In addition, considering the poorly constrained downdip limit of the seismogenic zone using geodetic observations, the unreleased slip deficit may in fact represent uncertainties, including the portion for interseismic stress relaxation and the temporal variation in locking width (K. Wang and Tréhu, 2016). Therefore, the discrepancy highlights the necessity of conducting dynamic simulations in addition to static calculations.

We further compared our results with the heterogeneous ruptures inferred from coastal subsidence estimates. P. L. Wang et al. (2013) proposed a range of heterogeneous slip models for the CE 1700 event using a 3D elastic dislocation model with reference to the subsidence estimates. Assuming the fault slip patches follow the bell-shaped function, they adjusted the slip patch parameters (e.g., size, location, and peak slip) to match the model-predicted surface deformation to the paleoseismic subsidence estimates using a trial-and-error approach. In particular, they preferred a model consisting of four high-slip patches for simplicity and having a reasonable fit with the observations. However, the models are limited by the large subsidence data gaps in northern and southern Cascadia (Figure 11).

In comparison, our scenarios incorporate the locking models utilizing Global Navigation Satellite System GNSS data, which are more densely spaced along Cascadia, as the physical constraints on rupture depth and heterogeneities. We demonstrate that three high-slip patches in a dynamic rupture model could be sufficient to generate subsidence amplitudes similar to the observation of the CE 1700 megathrust earthquake. Similarly, the Schmalzle locking-constrained earthquake sequence simulation (D. Li & Liu, 2021) also suggests a three high-slip patches scenario and its synthetic subsidence is in good agreement with the observational data. Therefore, the three high-slip patches scenarios could be close to the CE 1700 event.

5.4. Limitations in Deriving Future Coseismic Slip

Although our dynamic models produce reasonable ground motions that match with multiple observational studies, there are limitations in constraining the up-dip frictional properties and rupture behaviors. The first concern comes from the frictional behaviors of the frontal prism. In our model, the strength drop (difference between static and dynamic stress) at the frontal prism decreases toward the trench, and the initial stress equals the addition of dynamic stress and stress drop from static simulation. Although cohesion could suppress fault failure at the beginning of the simulations, the stress perturbations from ruptures could induce higher slip rates at shallow depths as it easily overcomes the small strength drop, especially with the dynamic effects of free-surface reflection. However, in reality, velocity-strengthening materials are known to slip at low rates. Our models do not consider the plastic deformation of the frontal prism either. Indeed, cohesion could partly describe the energy absorption close to the free surface caused by the presence of unconsolidated gouge and clays (Galvez et al., 2014). However, the amplitude of cohesion in our case is not constrained by laboratory experiments, including local mineralogy, lithology, and fluid pressure. Moreover, the frictional behaviors in our model are prescribed for the fault interface, and off-fault plasticity is neglected. Ulrich et al. (2022) and Wilson and Ma (2021) highlight the inelastic deformation of sediments as one of the dominant factors controlling seafloor deformation, hence tsunamic genesis. Incorporating off-fault plasticity and careful descriptions of frictional behaviors with respect to laboratory experiments and offshore geological studies would help establish realistic dynamic rupture scenarios.

Another major concern in estimating tsunami hazards comes from the uncertainty in future shallow rupture behavior. In our model, we assumed a simplified fault geometry where the fault extends to the top of the model domain, introducing trench-breaching ruptures in our dynamic models. Nevertheless, other rupture modes such as buried rupture, splay-faulting, and activation of thrusts and back-thrusts are possible (K. Wang and Tréhu, 2016). The orientation and angle of the splay faults cause notable changes in seafloor uplift and tsunami heights (Aslam et al., 2021), and D. Gao et al. (2018) constructed hypothetical splay-fault geometries in addition to Priest et al. (2009) and a continuous along-strike frontal thrust model based on seismic profiles. Therefore, a more detailed 3D mapping of the complex fault geometry could help evaluate the possibility of different rupture mechanisms using dynamic rupture simulations. Accordingly, this project can be further developed from multiple perspectives in the future, including the off-fault plasticity, the along-strike changes in accretionary prism geometry, and the addition of splay faults.

6. Conclusion

In this study, we conducted 3D dynamic rupture simulations for Cascadia using different interseismic locking models with a range of hypocenter locations in the South assuming constant effective normal stress. While the locking models have similar static moments and locking distributions, their heterogeneous stress distribution leads to distinct rupture scenarios. Both Schmalzle and Li models demonstrate that the south is capable of generating $M_w > 8$ segmented ruptures and FMR depending on the frictional parameters and hypocenter locations. For instance, both segmented and FMR can occur with the same hypocenter location given different frictional parameters.

We found that the heterogeneity of interseismic locking models plays a key role in determining the rupture process. The more heterogeneous Schmalzle locking model yields a stress distribution with more asperities, thus facilitating segmented ruptures on the high-stress asperities. These segmented ruptures appear to have a reasonable correlation with the along-strike extent of the inferred recurrence intervals. On the other hand, the more homogeneous Li locking model gives a smoother stress distribution, hence the scenarios are either FMR or self-arrested ruptures. The selection of hypocenter location is also a crucial parameter in controlling the potential segmentation patterns. For the more heterogeneous model, the scenarios initiated from the higher stress asperities demonstrate a significantly larger moment magnitude.

Accordingly, surface deformation is also largely controlled by these factors. While the homogeneous locking model results in a simpler coastal subsidence pattern with the largest subsidence in the region of highest slip and decreasing further away, the heterogeneous model gives a more complex pattern depending on the stress asperities. This also suggests that the CE 1700 earthquake may represent a possibly more heterogeneous slip model provided its fluctuating coastal subsidence pattern. In particular, our results show that a three high-slip patches scenario can reproduce a reasonably similar seafloor deformation with the CE 1700 earthquake. Apart from coastal subsidence, the synthetic ground shaking also demonstrates that rupture directivity is strongly controlled by prescribed hypocenter locations, leading to nearly double the PGV for scenarios initiated at different hypocenter locations even though the resulting slip distributions are almost the same.

Our simulation results can also be applied to tsunami modeling to evaluate the tsunami risks for each segmented rupture type. Furthermore, our models may help evaluate the present probabilistic seismic hazard analysis by providing possible slip distributions of the paleoearthquakes for source characterization as well as the synthetic ground motions for comparison with that generated by the empirical ground motion prediction equations.

In addition to specific investigations on Cascadia, our findings could help understand the general relationship between interseismic locking models and the possible earthquake slip patterns, thus the moment magnitudes. Our study together with the dynamic simulations for the other fault zones, such as the Nicoya Peninsula subduction megathrust (Yang, Yao, He, Newman, Weng, 2019) and the Anninghe fault (S. Yao and Yang, 2022), raises the possibility to provide new insights into more efficient slip estimations of seismic potentials for the fault zones worldwide in the future.

Data Availability Statement

All the data and software used in this work have been previously published. Dynamic rupture simulations were generated using the open-source software package PyLith, freely available at Aagaard et al. (2013c). Locking model data may be found in S. Li et al. (2018), Lindsey et al. (2021), and Schmalzle et al. (2014). All the important scripts and outputs from our study are openly available in Zenodo at https://doi.org/10.5281/zenodo.7940151.

References

Aagaard, B. T., Kientz, S., Knepley, M., Strand, L., & Williams, C. (2013a). *PyLith user manual, version 2.1.0*. Computational Infrastructure for Geodynamics. Retrieved from https://geodynamics.org/resources/pylith/supportingdocs

Aagaard, B. T., Knepley, M. G., & Williams, C. A. (2013b). A domain decomposition approach to implementing fault slip in finite-element models of quasi-static and dynamic crustal deformation. *Journal of Geophysical Research: Solid Earth*, *118*(6), 3059–3079. https://doi.org/10.1002/jgrb.50217

Aagaard, B. T., Knepley, M. G., & Williams, C. A. (2013c). PyLith v2.1.0 [software]. Computational Infrastructure of Geodynamics. Retrieved from https://geodynamics.org

Almeida, R., Lindsey, E. O., Bradley, K., Hubbard, J., Mallick, R., & Hill, E. M. (2018). Can the updip limit of frictional locking on megathrusts be detected geodetically? Quantifying the effect of stress shadows on near-trench coupling. *Geophysical Research Letters*, *45*(10), 4754–4763. https://doi.org/10.1029/2018GL077785

Aochi, H., & Madariaga, R. (2003). The 1999 Izmit, Turkey, earthquake: Nonplanar fault structure, dynamic rupture process, and strong ground motion. *Bulletin of the Seismological Society of America*, *93*(3), 1249–1266. https://doi.org/10.1785/0120020167

Aslam, K. S., Thomas, A. M., & Melgar, D. (2021). The effect of fore-arc deformation on shallow earthquake rupture behavior in the Cascadia subduction zone. *Geophysical Research Letters*, *48*(20), e2021GL093941. https://doi.org/10.1029/2021GL093941

Atwater, B. F., Carson, B., Griggs, G. B., Johnson, H. P., & Salmi, M. S. (2014). Rethinking turbidite paleoseismology along the Cascadia subduction zone. *Geology*, *42*(9), 827–830. https://doi.org/10.1130/G35902.1

Atwater, B. F., & Hemphill-Haley, E. (1997). *Recurrence intervals for great earthquakes of the past 3,500 years at northeastern Willapa Bay, Washington (No. 1576)*. US Government Printing Office. https://doi.org/10.3133/pp1576

Audet, P., Bostock, M. G., Christensen, N. I., & Peacock, S. M. (2009). Seismic evidence for overpressured subducted oceanic crust and megathrust fault sealing. *Nature*, *457*(7225), 76–78. https://doi.org/10.1038/nature07650

Baumann, C., & Dalguer, L. A. (2014). Evaluating the compatibility of dynamic rupture-based synthetic ground motion with empirical ground-motion prediction equation. *Bulletin of the Seismological Society of America*, *104*(2), 634–652. https://doi.org/10.1785/0120130077

Blacker, T. D., Owen, S. J., Staten, M. L., Quadros, W. R., Hanks, B., Clark, B. W., et al. (2016). CUBIT geometry and mesh generation toolkit 15.1 user documentation (No. SAND-2016-1649R) [Software]. Sandia National Lab. (SNL-NM), Albuquerque, NM (United States). https://doi.org/10.2172/1430472

Brocher, T. M. (2005). Empirical relations between elastic wavespeeds and density in the Earth's crust. *Bulletin of the Seismological Society of America*, *95*(6), 2081–2092. https://doi.org/10.1785/0120050077

Burgette, R. J., Weldon, R. J., & Schmidt, D. A. (2009). Interseismic uplift rates for western Oregon and along-strike variation in locking on the Cascadia subduction zone. *Journal of Geophysical Research*, *114*(B1), 2009-01. https://doi.org/10.1029/2008JB005679

Chen, X., & Yang, H. (2020). Effects of seismogenic width and low-velocity zones on estimating slip-weakening distance from near-fault ground deformation. *Geophysical Journal International*, *223*(3), 1497–1510. https://doi.org/10.1093/gji/ggaa385

Chen, X., Yang, H., & Jin, M. (2021). Inferring critical slip-weakening distance from near-fault accelerogram of the 2014 M_w 6.2 Ludian earthquake. *Seismological Research Letters*, *92*(6), 3416–3427. https://doi.org/10.1785/0220210089

Chounet, A., Vallée, M., Causse, M., & Courboulex, F. (2018). Global catalog of earthquake rupture velocities shows anticorrelation between stress drop and rupture velocity. *Tectonophysics*, *733*, 148–158. https://doi.org/10.1016/j.tecto.2017.11.005

Cocco, M., Tinti, E., Marone, C., & Piatanesi, A. (2009). Scaling of slip weakening distance with final slip during dynamic earthquake rupture. *International Geophysics*, *94*, 163–186. https://doi.org/10.1016/S0074-6142(08)00007-7

Courant, R., Friedrichs, K., & Lewy, H. (1967). On the partial difference equations of mathematical physics (P. Fox, Trans.). *IBM Journal of Research and Development*, *11*(2), 215–234. (Original work published 1928) https://doi.org/10.1147/rd.112.0215

Day, S. M., Dalguer, L. A., Lapusta, N., & Liu, Y. (2005). Comparison of finite difference and boundary integral solutions to three-dimensional spontaneous rupture. *Journal of Geophysical Research*, *110*(B12), B12307. https://doi.org/10.1029/2005JB003813

Dieterich, J. H. (1986). A model for the nucleation of earthquake slip. *Earthquake source mechanics*, *37*, 37–47. https://doi.org/10.1029/GM037p0037

Di Toro, G., Han, R., Hirose, T., De Paola, N., Nielsen, S., Mizoguchi, K., et al. (2011). Fault lubrication during earthquakes. *Nature*, *471*(7339), 494–498. https://doi.org/10.1038/nature09838

Duan, B. (2012). Dynamic rupture of the 2011 M_w 9.0 Tohoku-Oki earthquake: Roles of a possible subducting seamount. *Journal of Geophysical Research*, *117*(B5), 05311. https://doi.org/10.1029/2011JB009124

Engelhart, S. E., Vacchi, M., Horton, B. P., Nelson, A. R., & Kopp, R. E. (2015). A sea-level database for the Pacific coast of central North America. *Quaternary Science Reviews*, *113*, 78–92. https://doi.org/10.1016/j.quascirev.2014.12.001

Flück, P., Hyndman, R. D., & Wang, K. (1997). Three-dimensional dislocation model for great earthquakes of the Cascadia subduction zone. *Journal of Geophysical Research*, *102*(B9), 20539–20550. https://doi.org/10.1029/97JB01642

Frankel, A., Chen, R., Petersen, M., Moschetti, M., & Sherrod, B. (2015). 2014 update of the Pacific Northwest portion of the US National seismic hazard maps. *Earthquake Spectra*, *31*(1_suppl), S131–S148. https://doi.org/10.1193/111314EQS193M

Fujiwara, T., dos Santos Ferreira, C., Bachmann, A. K., Strasser, M., Wefer, G., Sun, T., et al. (2017). Seafloor displacement after the 2011 Tohoku-Oki earthquake in the northern Japan trench examined by repeated bathymetric surveys. *Geophysical Research Letters*, *44*(23), 11-833. https://doi.org/10.1002/2017GL075839

Fukuyama, E., & Mikumo, T. (2007). Slip-weakening distance estimated at near-fault stations. *Geophysical Research Letters*, *34*(9), L09302. https://doi.org/10.1029/2006GL029203

Galis, M., Pelties, C., Kristek, J., Moczo, P., Ampuero, J. P., & Mai, P. M. (2015). On the initiation of sustained slip-weakening ruptures by localized stresses. *Geophysical Journal International*, *200*(2), 890–909. https://doi.org/10.1093/gji/ggu436

Gallovič, F., Valentová, Ľ., Ampuero, J. P., & Gabriel, A. A. (2019). Bayesian dynamic finite-fault inversion: 2. Application to the 2016 M_w 6.2 Amatrice, Italy, earthquake. *Journal of Geophysical Research: Solid Earth*, *124*(7), 6970–6988. https://doi.org/10.1029/2019JB017512

Galvez, P., Ampuero, J. P., Dalguer, L. A., Somala, S. N., & Nissen-Meyer, T. (2014). Dynamic earthquake rupture modelled with an unstructured 3-D spectral element method applied to the 2011 M 9 Tohoku earthquake. *Geophysical Journal International*, *198*(2), 1222–1240. https://doi.org/10.1093/gji/ggu203

Gao, D., Wang, K., Insua, T. L., Sypus, M., Riedel, M., & Sun, T. (2018). Defining megathrust tsunami source scenarios for northernmost Cascadia. *Natural Hazards*, *94*(1), 445–469. https://doi.org/10.1007/s11069-018-3397-6

Gao, X., & Wang, K. (2014). Strength of stick-slip and creeping subduction megathrusts from heat flow observations. *Science*, *345*(6200), 1038–1041. https://doi.org/10.1126/science.1255487

Gao, X., & Wang, K. (2017). Rheological separation of the megathrust seismogenic zone and episodic tremor and slip. *Nature*, *543*(7645), 416–419. https://doi.org/10.1038/nature21389

Gnedin, N. Y., Semenov, V. A., & Kravtsov, A. V. (2018). Enforcing the Courant–Friedrichs–Lewy condition in explicitly conservative local time stepping schemes. *Journal of Computational Physics*, *359*, 93–105. https://doi.org/10.1016/j.jcp.2018.01.008

Goldberg, D. E., Melgar, D., Hayes, G. P., Crowell, B. W., & Sahakian, V. J. (2021). A ground-motion model for GNSS peak ground displacement. *Bulletin of the Seismological Society of America*, *111*(5), 2393–2407. https://doi.org/10.1785/0120210042

Goldfinger, C., Galer, S., Beeson, J., Hamilton, T., Black, B., Romsos, C., et al. (2017). The importance of site selection, sediment supply, and hydrodynamics: A case study of submarine paleoseismology on the northern Cascadia margin, Washington USA. *Marine Geology*, *384*, 4–46. https://doi.org/10.1016/j.margeo.2016.06.008

Goldfinger, C., Nelson, C. H., Morey, A. E., Johnson, J. R., Patton, J., Karabanov, E., et al. (2012). Turbidite event history—Methods and implications for Holocene paleoseismicity of the Cascadia subduction zone. In *U.S. Geological survey professional paper 1661–F, 170 p., 64 figures*. Retrieved from http://pubs.usgs.gov/pp/pp1661/f

Han, S., Bangs, N. L., Carbotte, S. M., Saffer, D. M., & Gibson, J. C. (2017). Links between sediment consolidation and Cascadia megathrust slip behaviour. *Nature Geoscience*, *10*(12), 954–959. https://doi.org/10.1038/s41561-017-0007-2

Harris, R. A., Barall, M., Aagaard, B., Ma, S., Roten, D., Olsen, K., et al. (2018). A suite of exercises for verifying dynamic earthquake rupture codes. *Seismological Research Letters*, *89*(3), 1146–1162. https://doi.org/10.1785/0220170222

Hyndman, R. D., & Wang, K. (1995). The rupture zone of Cascadia great earthquakes from current deformation and the thermal regime. *Journal of Geophysical Research*, *100*(B11), 22133–22154. https://doi.org/10.1029/95JB01970

Ida, Y. (1972). Cohesive force across the tip of a longitudinal-shear crack and Griffith's specific surface energy. *Journal of Geophysical Research*, *77*(20), 3796–3805. https://doi.org/10.1029/JB077i020p03796

Ide, S., & Aochi, H. (2005). Earthquakes as multiscale dynamic ruptures with heterogeneous fracture surface energy. *Journal of Geophysical Research*, *110*(B11), 2005. https://doi.org/10.1029/2004JB003591

Ide, S., & Aochi, H. (2013). Historical seismicity and dynamic rupture process of the 2011 Tohoku-Oki earthquake. *Tectonophysics*, *600*, 1–13. https://doi.org/10.1016/j.tecto.2012.10.018

Igel, H. (2017). *Computational seismology: A practical introduction*. Oxford University Press.

Ihlenburg, F., & Babuška, I. (1995). Dispersion analysis and error estimation of Galerkin finite element methods for the Helmholtz equation. *International Journal for Numerical Methods in Engineering*, *38*(22), 3745–3774. https://doi.org/10.1002/nme.1620382203

Kaneko, Y., Fukuyama, E., & Hamling, I. J. (2017). Slip-weakening distance and energy budget inferred from near-fault ground deformation during the 2016 M_w 7. 8 Kaikōura earthquake. *Geophysical Research Letters*, *44*(10), 4765–4773. https://doi.org/10.1002/2017GL073681

Kelsey, H. M., Nelson, A. R., Hemphill-Haley, E., & Witter, R. C. (2005). Tsunami history of an Oregon coastal lake reveals a 4600 yr record of great earthquakes on the Cascadia subduction zone. *Geological Society of America Bulletin*, *117*(7–8), 1009–1032. https://doi.org/10.1130/B25452.1

Kuo, L. W., Li, H., Smith, S. A., Di Toro, G., Suppe, J., Song, S. R., et al. (2014). Gouge graphitization and dynamic fault weakening during the 2008 M_w 7.9 Wenchuan earthquake. *Geology*, *42*(1), 47–50. https://doi.org/10.1130/G34862.1

Lamb, S. (2006). Shear stresses on megathrusts: Implications for mountain building behind subduction zones. *Journal of Geophysical Research*, *111*(B7), B07401. https://doi.org/10.1029/2005JB003916

Lambert, V., Lapusta, N., & Faulkner, D. (2021). Scale dependence of earthquake rupture prestress in models with enhanced weakening: Implications for event statistics and inferences of fault stress. *Journal of Geophysical Research: Solid Earth*, *126*(10), e2021JB021886. https://doi.org/10.1029/2021JB021886

Lapusta, N., & Liu, Y. (2009). Three-dimensional boundary integral modeling of spontaneous earthquake sequences and aseismic slip. *Journal of Geophysical Research*, *114*(B9), B09303. https://doi.org/10.1029/2008JB005934

Lay, T., Kanamori, H., Ammon, C. J., Koper, K. D., Hutko, A. R., Ye, L., et al. (2012). Depth-varying rupture properties of subduction zone megathrust faults. *Journal of Geophysical Research*, *117*(B4), B04311. https://doi.org/10.1029/2011JB009133

Li, D., & Liu, Y. (2021). Cascadia megathrust earthquake rupture model constrained by geodetic fault locking. *Philosophical Transactions of the Royal Society A*, *379*(2196), 20200135. https://doi.org/10.1098/rsta.2020.0135

Li, D., McGuire, J. J., Liu, Y., & Hardebeck, J. L. (2018). Stress rotation across the Cascadia megathrust requires a weak subduction plate boundary at seismogenic depths. *Earth and Planetary Science Letters*, *485*, 55–64. https://doi.org/10.1016/j.epsl.2018.01.002

Li, S., Wang, K., Wang, Y., Jiang, Y., & Dosso, S. E. (2018). Geodetically inferred locking state of the Cascadia megathrust based on a viscoelastic Earth model [Dataset]. Journal of Geophysical Research: Solid Earth, *123*(9), 8056–8072. https://doi.org/10.1029/2018JB015620

Li, Y., Song, X., Shan, X., Qu, C., & Wang, Z. (2016). Locking degree and slip rate deficit distribution on MHT fault before 2015 Nepal M_w 7.9 earthquake. *Journal of Asian Earth Sciences*, *119*, 78–86. https://doi.org/10.1016/j.jseaes.2016.01.011

Lindsey, E. O., Mallick, R., Hubbard, J. A., Bradley, K. E., Almeida, R. V., Moore, J. D., et al. (2021). Slip rate deficit and earthquake potential on shallow megathrusts [Dataset]. Nature Geoscience, *14*(5), 321–326. https://doi.org/10.1038/s41561-021-00736-x

Long, A. J., & Shennan, I. (1998). Models of rapid relative sea-level change in Washington and Oregon, USA. *The Holocene*, *8*(2), 129–142. https://doi.org/10.1191/095968398666306493

Madden, E. H., Ulrich, T., & Gabriel, A. A. (2022). The state of pore fluid pressure and 3-D megathrust earthquake dynamics. *Journal of Geophysical Research: Solid Earth*, *127*(4), e2021JB023382. https://doi.org/10.1029/2021JB023382

Marone, C., & Kilgore, B. (1993). Scaling of the critical slip distance for seismic faulting with shear strain in fault zones. *Nature*, *362*(6421), 618–621. https://doi.org/10.1038/362618a0

Materna, K., Bartlow, N., Wech, A., Williams, C., & Bürgmann, R. (2019). Dynamically triggered changes of plate interface coupling in Southern Cascadia. *Geophysical Research Letters*, *46*(22), 12890–12899. https://doi.org/10.1029/2019GL084395

Maurer, J., Segall, P., & Bradley, A. M. (2017). Bounding the moment deficit rate on crustal faults using geodetic data: Methods. *Journal of Geophysical Research: Solid Earth*, *122*(8), 6811–6835. https://doi.org/10.1002/2017JB014300

McCaffrey, R., King, R. W., Payne, S. J., & Lancaster, M. (2013). Active tectonics of northwestern US inferred from GPS-derived surface velocities. *Journal of Geophysical Research: Solid Earth*, *118*(2), 709–723. https://doi.org/10.1029/2012JB009473

McCrory, P. A., Blair, J. L., Oppenheimer, D. H., & Walter, S. R. (2004). Depth to the Juan de Fuca slab beneath the Cascadia subduction margin: A 3-D model for sorting earthquakes [Dataset]. Data Series. https://doi.org/10.3133/ds91

McCrory, P. A., Hyndman, R. D., & Blair, J. L. (2014). Relationship between the Cascadia fore-arc mantle wedge, nonvolcanic tremor, and the downdip limit of seismogenic rupture. *Geochemistry, Geophysics, Geosystems*, *15*(4), 1071–1095. https://doi.org/10.1002/2013GC005144

Melgar, D. (2021). Was the January 26th, 1700 Cascadia earthquake part of a rupture sequence? *Journal of Geophysical Research: Solid Earth*, *126*(10), e2021JB021822. https://doi.org/10.1029/2021JB021822

Michel, S., Avouac, J. P., Lapusta, N., & Jiang, J. (2017). Pulse-like partial ruptures and high-frequency radiation at creeping-locked transition during megathrust earthquakes. *Geophysical Research Letters*, *44*(16), 8345–8351. https://doi.org/10.1002/2017GL074725

Michel, S., Gualandi, A., & Avouac, J. P. (2019). Interseismic coupling and slow slip events on the Cascadia megathrust. *Pure and Applied Geophysics*, *176*(9), 3867–3891. https://doi.org/10.1007/s00024-018-1991-x

Mikumo, T., Olsen, K. B., Fukuyama, E., & Yagi, Y. (2003). Stress-breakdown time and slip-weakening distance inferred from slip-velocity functions on earthquake faults. *Bulletin of the Seismological Society of America*, *93*(1), 264–282. https://doi.org/10.1785/0120020082

Montalva, G. A., Bastías, N., & Leyton, F. (2022). Strong ground motion prediction model for PGV and spectral velocity for the Chilean subduction zone. *Bulletin of the Seismological Society of America*, *112*(1), 348–360. https://doi.org/10.1785/0120210037

Moreno, M., Rosenau, M., & Oncken, O. (2010). 2010 Maule earthquake slip correlates with pre-seismic locking of Andean subduction zone. *Nature*, *467*(7312), 198–202. https://doi.org/10.1038/nature09349

Nur, A. (1978). Nonuniform friction as a physical basis for earthquake mechanics. *Pure and Applied Geophysics*, *116*(4), 964–989. https://doi.org/10.1007/BF00876550

Ohnaka, M. (2003). A constitutive scaling law and a unified comprehension for frictional slip failure, shear fracture of intact rock, and earthquake rupture. *Journal of Geophysical Research*, *108*(B2), 2080. https://doi.org/10.1029/2000JB000123

Petersen, M. D., Moschetti, M. P., Powers, P. M., Mueller, C. S., Haller, K. M., Frankel, A. D., et al. (2014). Documentation for the 2014 update of the United States national seismic hazard maps. In *U.S. Geological Survey open-file report 2014-1091* (p. 243). https://doi.org/10.3133/ofr20141091

Pollitz, F. F., & Evans, E. L. (2017). Implications of the earthquake cycle for inferring fault locking on the Cascadia megathrust. *Geophysical Journal International*, *209*(1), 167–185. https://doi.org/10.1093/gji/ggx009

Priest, G. R., Goldfinger, C., Wang, K., Witter, R. C., Zhang, Y., & Baptista, A. M. (2009). Tsunami hazard assessment of the Northern Oregon coast: A multi-deterministic approach tested at Cannon Beach, Clatsop County, Oregon. In *Oregon Department of Geology Mineral Industries Special Paper* (Vol. 41, p. 87).

Ramos, M. D., & Huang, Y. (2019). How the transition region along the Cascadia megathrust influences coseismic behavior: Insights from 2-D dynamic rupture simulations. *Geophysical Research Letters*, *46*(4), 1973–1983. https://doi.org/10.1029/2018GL080812

Ramos, M. D., Huang, Y., Ulrich, T., Li, D., Gabriel, A. A., & Thomas, A. M. (2021). Assessing margin-wide rupture behaviors along the Cascadia megathrust with 3-D dynamic rupture simulations. *Journal of Geophysical Research: Solid Earth*, *126*(7), e2021JB022005. https://doi.org/10.1029/2021JB022005

Rice, J. R. (1992). Fault stress states, pore pressure distributions, and the weakness of the San Andreas fault. In *International geophysics* (Vol. 51, pp. 475–503). Academic Press. https://doi.org/10.1016/S0074-6142(08)62835-1

Rogers, G., & Dragert, H. (2003). Episodic tremor and slip on the Cascadia subduction zone: The chatter of silent slip. *Science*, *300*(5627), 1942–1943. https://doi.org/10.1126/science.1084783

Rowe, C. D., & Griffith, W. A. (2015). Do faults preserve a record of seismic slip: A second opinion. *Journal of Structural Geology*, *78*, 1–26. https://doi.org/10.1016/j.jsg.2015.06.006

Saffer, D. M., & Tobin, H. J. (2011). Hydrogeology and mechanics of subduction zone forearcs: Fluid flow and pore pressure. *Annual Review of Earth and Planetary Sciences*, *39*(1), 157–186. https://doi.org/10.1146/annurev-earth-040610-133408

Satake, K., Wang, K., & Atwater, B. F. (2003). Fault slip and seismic moment of the 1700 Cascadia earthquake inferred from Japanese tsunami descriptions. *Journal of Geophysical Research*, *108*(B11), 2535. https://doi.org/10.1029/2003JB002521

Schmalzle, G. M., McCaffrey, R., & Creager, K. C. (2014). Central Cascadia subduction zone creep [Dataset]. Geochemistry, Geophysics, Geosystems, *15*(4), 1515–1532. https://doi.org/10.1002/2013GC005172

Semblat, J. F., & Brioist, J. J. (2000). Efficiency of higher order finite elements for the analysis of seismic wave propagation. *Journal of Sound and Vibration*, *231*(2), 460–467. https://doi.org/10.48550/arXiv.0901.3715

Semblat, J. F., Lenti, L., & Gandomzadeh, A. (2011). A simple multi-directional absorbing layer method to simulate elastic wave propagation in unbounded domains. *International Journal for Numerical Methods in Engineering*, *85*(12), 1543–1563. https://doi.org/10.1002/nme.3035

Shi, Z., & Day, S. M. (2013). Rupture dynamics and ground motion from 3-D rough-fault simulations. *Journal of Geophysical Research: Solid Earth*, *118*(3), 1122–1141. https://doi.org/10.1002/jgrb.50094

Simons, M., Minson, S. E., Sladen, A., Ortega, F., Jiang, J., Owen, S. E., et al. (2011). The 2011 magnitude 9.0 Tohoku-Oki earthquake: Mosaicking the megathrust from seconds to centuries. *Science*, *332*(6036), 1421–1425. https://doi.org/10.1126/science.1206731

Somerville, P. G., Smith, N. F., Graves, R. W., & Abrahamson, N. A. (1997). Modification of empirical strong ground motion attenuation relations to include the amplitude and duration effects of rupture directivity. *Seismological Research Letters*, *68*(1), 199–222. https://doi.org/10.1785/gssrl.68.1.199

Stanislowski, K., Roesner, A., & Ikari, M. J. (2022). Implications for megathrust slip behavior and pore pressure at the shallow northern Cascadia subduction zone from laboratory friction experiments. *Earth and Planetary Science Letters*, *578*, 117297. https://doi.org/10.1016/j.epsl.2021.117297

Stephenson, W. J., Reitman, N. G., & Angster, S. J. (2017). P-And S-wave velocity models incorporating the Cascadia subduction zone for 3D earthquake ground motion simulations, version 1.6—Update for open-file report 2007–1348 (No. 2017-1152). *US Geological Survey*. https://doi.org/10.3133/ofr20171152

Tréhu, A. M., Blakely, R. J., & Williams, M. C. (2012). Subducted seamounts and recent earthquakes beneath the central Cascadia forearc. *Geology*, *40*(2), 103–106. https://doi.org/10.1130/G32460.1

Ulrich, T., Gabriel, A. A., & Madden, E. H. (2022). Stress, rigidity and sediment strength control megathrust earthquake and tsunami dynamics. *Nature Geoscience*, *15*, 1–7. https://doi.org/10.1038/s41561-021-00863-5

Viesca, R. C., & Garagash, D. I. (2015). Ubiquitous weakening of faults due to thermal pressurization. *Nature Geoscience*, *8*(11), 875–879. https://doi.org/10.1038/ngeo2554

Walton, M. A., Staisch, L. M., Dura, T., Pearl, J. K., Sherrod, B., Gomberg, J., et al. (2021). Toward an integrative geological and geophysical view of Cascadia subduction zone earthquakes. *Annual Review of Earth and Planetary Sciences*, *49*(1), 367–398. https://doi.org/10.1146/annurev-earth-071620-065605

Wang, K., Hu, Y., & He, J. (2012). Deformation cycles of subduction earthquakes in a viscoelastic Earth. *Nature*, *484*(7394), 327–332. https://doi.org/10.1038/nature11032

Wang, K., & Tréhu, A. M. (2016). Invited review paper: Some outstanding issues in the study of great megathrust earthquakes—The Cascadia example. *Journal of Geodynamics*, *98*, 1–18. https://doi.org/10.1016/j.jog.2016.03.010

Wang, K., Wells, R., Mazzotti, S., Hyndman, R. D., & Sagiya, T. (2003). A revised dislocation model of interseismic deformation of the Cascadia subduction zone. *Journal of Geophysical Research*, *108*(B1), 2026. https://doi.org/10.1029/2001JB001227

Wang, P. L., Engelhart, S. E., Wang, K., Hawkes, A. D., Horton, B. P., Nelson, A. R., & Witter, R. C. (2013). Heterogeneous rupture in the great Cascadia earthquake of 1700 inferred from coastal subsidence estimates. *Journal of Geophysical Research: Solid Earth*, *118*(5), 2460–2473. https://doi.org/10.1002/jgrb.50101

Watt, J. T., & Brothers, D. S. (2021). Systematic characterization of morphotectonic variability along the Cascadia convergent margin: Implications for shallow megathrust behavior and tsunami hazards. *Geosphere*, *17*(1), 95–117. https://doi.org/10.1130/GES02178.1

Wells, D. L., & Coppersmith, K. J. (1994). New empirical relationships among magnitude, rupture length, rupture width, rupture area, and surface displacement. *Bulletin of the Seismological Society of America*, *84*(4), 974–1002. https://doi.org/10.1785/BSSA0840040974

Weng, H., & Ampuero, J. P. (2020). Continuum of earthquake rupture speeds enabled by oblique slip. *Nature Geoscience*, *13*(12), 817–821. https://doi.org/10.1038/s41561-020-00654-4

Weng, H., & Yang, H. (2018). Constraining frictional properties on fault by dynamic rupture simulations and near-field observations. *Journal of Geophysical Research: Solid Earth*, *123*(8), 6658–6670. https://doi.org/10.1029/2017JB015414

Wilson, A., & Ma, S. (2021). Wedge plasticity and fully coupled simulations of dynamic rupture and tsunami in the Cascadia subduction zone. *Journal of Geophysical Research: Solid Earth*, *126*(7), e2020JB021627. https://doi.org/10.1029/2020JB021627

Wirth, E. A., & Frankel, A. D. (2019). Impact of down-dip rupture limit and high-stress drop subevents on coseismic land-level change during Cascadia Megathrust Earthquakes. *Bulletin of the Seismological Society of America*, *109*(6), 2187–2197. https://doi.org/10.1785/0120190043

Wirth, E. A., Frankel, A. D., Marafi, N., Vidale, J. E., & Stephenson, W. J. (2018). Broadband synthetic seismograms for magnitude 9 earthquakes on the Cascadia megathrust based on 3D simulations and stochastic synthetics, Part 2: Rupture parameters and variability. *Bulletin of the Seismological Society of America*, *108*(5A), 2370–2388. https://doi.org/10.1785/0120180029

Witter, R. C., Zhang, Y., Wang, K., Goldfinger, C., Priest, G. R., & Allan, J. C. (2012). Coseismic slip on the southern Cascadia megathrust implied by tsunami deposits in an Oregon lake and earthquake-triggered marine turbidites. *Journal of Geophysical Research*, *117*(B10), 10303. https://doi.org/10.1029/2012JB009404

Xin, D., & Zhang, Z. (2021). On the comparison of seismic ground motion simulated by physics-based dynamic rupture and predicted by empirical attenuation equations. *Bulletin of the Seismological Society of America*, *111*(5), 2595–2616. https://doi.org/10.1785/0120210077

Xu, J., Zhang, H., & Chen, X. (2015). Rupture phase diagrams for a planar fault in 3-D full-space and half-space. *Geophysical Journal International*, *202*(3), 2194–2206. https://doi.org/10.1093/gji/ggv284

Yang, H., Yao, S., He, B., & Newman, A. V. (2019). Earthquake rupture dependence on hypocentral location along the Nicoya Peninsula subduction megathrust. *Earth and Planetary Science Letters*, *520*, 10–17. https://doi.org/10.1016/j.epsl.2019.05.030

Yang, H., Yao, S., He, B., Newman, A. V., & Weng, H. (2019). Deriving rupture scenarios from interseismic locking distributions along the subduction megathrust. *Journal of Geophysical Research: Solid Earth*, *124*(10), 10376–10392. https://doi.org/10.1029/2019JB017541

Yao, H., Shearer, P. M., & Gerstoft, P. (2013). Compressive sensing of frequency-dependent seismic radiation from subduction zone megathrust ruptures. *Proceedings of the National Academy of Sciences*, *110*(12), 4512–4517. https://doi.org/10.1073/pnas.1212790110

Yao, S., & Yang, H. (2022). Hypocentral dependent shallow slip distribution and rupture extents along a strike-slip fault. *Earth and Planetary Science Letters*, *578*, 117296. https://doi.org/10.1016/j.epsl.2021.117296

Yao, S., & Yang, H. (2023). Towards ground motion prediction for potential large earthquakes from interseismic locking models. *Earth and Planetary Science Letters*, *601*, 117905. https://doi.org/10.1016/j.epsl.2022.117905

Ye, L., Lay, T., Kanamori, H., & Rivera, L. (2016). Rupture characteristics of major and great ($M_w \geq 7.0$) megathrust earthquakes from 1990 to 2015: 2. Depth dependence. *Journal of Geophysical Research: Solid Earth*, *121*(2), 845–863. https://doi.org/10.1002/2015JB012427

Zhang, W., Iwata, T., & Irikura, K. (2010). Dynamic simulation of the 1999 Chi-Chi, Taiwan, earthquake. *Journal of Geophysical Research*, *115*(B4), B04305. https://doi.org/10.1029/2008JB006201